

2D Janus Niobium Oxydihalide NbOXY: Multifunctional High-Mobility Piezoelectric Semiconductor for Electronics, Photonics and Sustainable Energy Applications

Tong Su,^{1,2,3} Ching Hua Lee,⁴ San-Dong Guo,⁵ Guangzhao Wang,⁶ Wee-Liat Ong,^{7,8} Liemao Cao,⁹ Weiwei Zhao,^{1,2,*} Shengyuan A. Yang,³ and Yee Sin Ang^{3,†}

¹*Savage Laboratory for Smart Materials, School of Materials Science and Engineering, Harbin Institute of Technology, Shenzhen 518055, China*

²*Shenzhen Key Laboratory of Flexible Printed Electronics Technology, Harbin Institute of Technology, Shenzhen 518055, China*

³*Science, Mathematics and Technology, Singapore University of Technology and Design, Singapore 487372*

⁴*Department of Physics, National University of Singapore, Singapore 117542*

⁵*School of Electronic Engineering, Xi'an University of Posts and Telecommunications, Xi'an 710121, China*

⁶*Key Laboratory of Extraordinary Bond Engineering and Advanced Materials Technology of Chongqing, School of Electronic Information Engineering, Yangtze Normal University, Chongqing 408100, China*

⁷*ZJU-UIUC Institute, College of Energy Engineering, Zhejiang University, Jiaxing, Haining, Zhejiang, 314400, China*

⁸*State Key Laboratory of Clean Energy Utilization, Zhejiang University, Hangzhou, Zhejiang, 310027, China*

⁹*College of Physics and Electronic Engineering, Hengyang Normal University, Hengyang 421002, China*

Two-dimensional (2D) niobium oxydihalide NbOI₂ has been recently demonstrated as an excellent in-plane piezoelectric and nonlinear optical material. Here we show that Janus niobium oxydihalide, NbOXY (X, Y = Cl, Br, I and X≠Y), is a multifunctional anisotropic semiconductor family with exceptional piezoelectric, electronic, photocatalytic and optical properties. NbOXY are stable and flexible monolayers with band gap around the visible light regime of ~ 1.9 eV. The anisotropic carrier mobility of NbOXY lies in the range of $10^3 \sim 10^4$ cm²V⁻¹s⁻¹, which represents some of the highest among 2D semiconductors of bandgap $\gtrsim 2$ eV. Inversion symmetry breaking in Janus NbOXY generates sizable out-of-plane d_{31} piezoelectric response while still retaining a strong in-plane piezoelectricity. Remarkably, NbOXY exhibits an additional out-of-plane piezoelectric response, d_{32} as large as 0.55 pm/V. G₀W₀-BSE calculation further reveals the strong linear optical dichroism of NbOXY in the visible-to-ultraviolet regime. The optical absorption peaks of 14 \sim 18 % in the deep UV regime (5 \sim 6 eV) outperform the vast majority of other 2D materials. The high carrier mobility, strong optical absorption, sizable built-in electric field and band alignment compatible with overall water splitting further suggest the strengths of NbOXY in solar-to-hydrogen conversion. We further propose a directional stress sensing device to demonstrate how the out-of-plane piezoelectricity can be harnessed for functional device applications. Our findings unveil NbOXY as an exceptional multifunctional 2D semiconductor for flexible electronics, optoelectronics, UV photonics, piezoelectronics and sustainable energy applications.

I. INTRODUCTION

Piezoelectricity is a phenomenon in which electrical (mechanical) signals are generated in a material in response to an external mechanical (electrical) stimuli. Piezoelectric materials, including crystals [1], polymer [2], bi-molecules [3] and 2D materials [4], play a critical role in electromechanical and mechano-electrical device technology, such as sensors and actuators [5–10]. Alongside with solid-state energy conversion strategies, such as solar cell [11], thermoelectricity [12] and triboelectricity [13], piezoelectricity represents another promising contender for salvaging electrical energy from mechanical motion [14]. Materials with simultaneous presence of excellent piezoelectric, electrical, mechanical and optical properties are particularly much sought-after due

to their enormous technological usefulness for developing *multifunctional* devices that synergize piezoelectricity with other functionalities.

Two-dimensional (2D) materials offer an exciting platform for the development of next-generation piezoelectronic technology [1, 16]. The atomically-thin nature of 2D materials and the enormous design space uniquely enabled by van der Waals heterostructure engineering [17, 18] offer a new paradigm for designing ultimately-compact and high-performance piezoelectric devices in the *2D Flatland*. Myriads of 2D in-plane and out-of-plane piezoelectric materials have been reported recently [19], including TMDCs [14, 20–24], hBN [25], graphene nitride [26]), α -In₂Se₃, doped graphene [27], and multilayer MoS₂ on PbTiO₃ [28]). The existence 2D materials with *simultaneous* in-plane and out-of-plane piezoelectricity, such as Janus transition metal dichalcogenides (TMDCs) [29, 30], Janus silicon dichalcogenide [31] as well as III-V [32, 33] and Janus III-VI monolayers [34, 35], further enriches the application potential of 2D piezoelec-

* Corresponding Author. wzhao@hit.edu.cn

† Corresponding Author. yeesin.ang@sutd.edu.sg

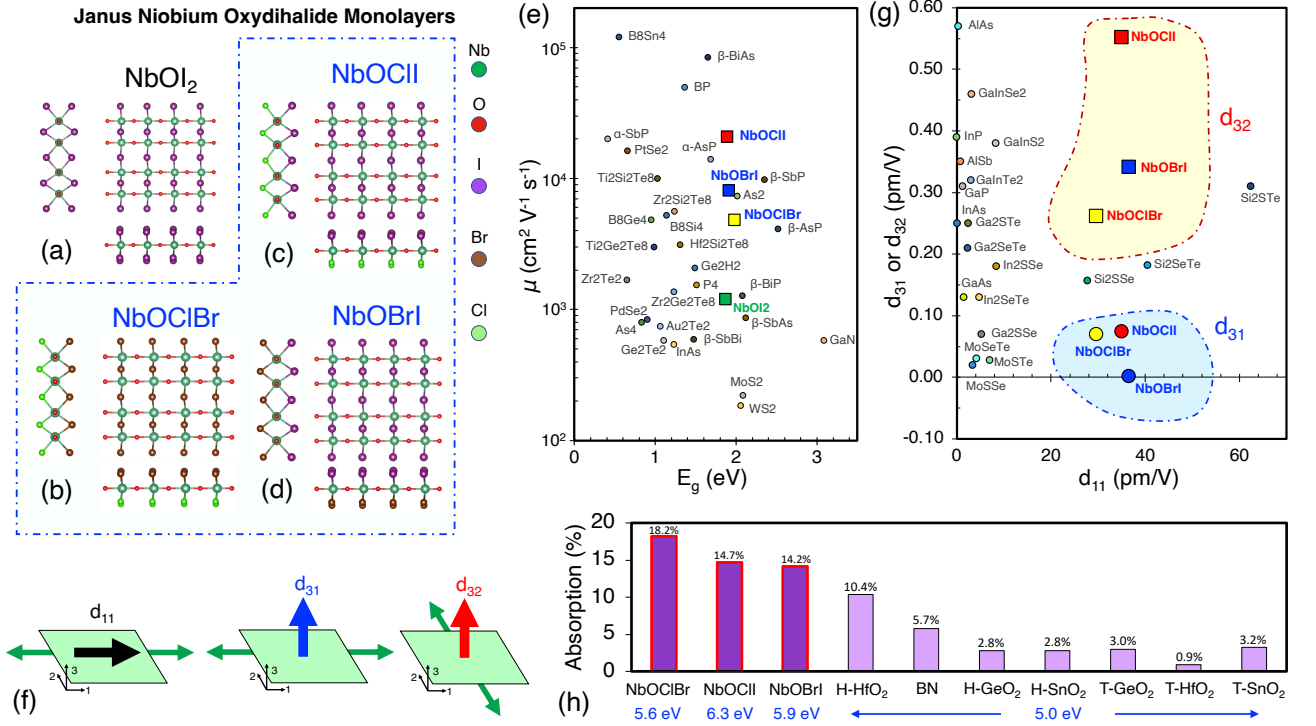


FIG. 1. **Lattice structures and highlights of the electrical, piezoelectronic and optical properties of Janus NbOXY.** (a) to (d) shows the lattice structures of non-Janus NbOI₂ and the Janus monolayers of NbOCIBr, NbOCII, NbOBrI, respectively, in which the inversion symmetry in the out-of-plane direction is broken due to the nonequivalent halogen atoms. (e) Comparison of electrical mobility of various 2D semiconductors obtained from DFT calculations. The NbOXY monolayers mobility is in the range of $10^3 \sim 10^4$ cm²V⁻¹s⁻¹. (f) Schematic drawings of the d_{11} , d_{31} and d_{32} piezoelectric responses. The thin arrows (green) denote the direction of mechanical stress and the thick arrows (black, blue and red) denote the direction of the electric charge polarization (d_{11} , d_{31} , d_{32}). (g) Piezoelectric responses d_{11} and d_{31} (or d_{32}) for various 2D materials. (h) Peak optical absorbance of NbOXY in comparison of other 2D materials [15]. The frequency of the peak absorbance are marked in blue font directly below the monolayer labels.

tric materials. The *directionally decoupled* nature of the mechanical stimuli and the corresponding electrical responses is particularly useful due to their compatibility with the stacking design of conventional CMOS and van der Waals heterostructure engineering [36].

Recent high throughput searches [37, 38] has established niobium oxydihalide monolayers (NbOX₂, X = Cl, Br, or I) as an exceptional piezoelectric 2D material family. Monolayer NbOI₂ – an experimentally [39, 40] fabricated air-stable 2D semiconductors with anisotropic electrical, mechanical and optical properties [41–43] – has an exceedingly large piezoelectric response of $d_{11} \approx 45$ pm/V. Out-of-plane piezoelectricity is, however, strictly forbidden in the NbOX₂ monolayer family due to the lattice centrosymmetry, which severely limits the potential of NbOX₂ in piezoelectric device applications. The absence of out-of-plane piezoelectricity in NbOI₂ immediately raises the following questions: Can inversion symmetry breaking from *Janus phase engineering* [29, 30] be used as an efficient way to generate sizable out-of-plane and in-plane piezoelectric response? Apart from the commonly observed d_{31} piezoelectric response, can other types of out-of-plane piezoelectricity, such as

d_{32} response, exist in Janus niobium oxydihalide monolayers? Will the electrical and optical properties of Janus niobium oxydihalide monolayers be beneficial for solid-state device applications, in addition to piezoelectricity?

In this work, we show that Janus-engineered niobium oxyhalide monolayer, NbOXY where X and Y are the halogen atoms Br, Cl, I, and $X \neq Y$, is a multifunctional semiconductor with ultrahigh carrier mobility, mechanical flexibility, strong optical dichroism, broadband visible and strong UV light absorption, compatibility with overall photocatalytic water splitting and simultaneous presence of in-plane and out-of-plane piezoelectricity (see Fig. 1 for the crystal structures and a highlight of the electrical, piezoelectric and optical properties of NbOXY). Using first-principle density functional theory (DFT) calculations, we show that NbOXY is dynamically, thermally and mechanically stable with excellent mechanical flexibility. The band gap of 2 eV, which lies in the visible light regime, and the large anisotropic [44, 45] carrier mobility, ranging from $10^{-1} \sim 10^4$ cm²V⁻¹s⁻¹ with NbOCII reaching well over 2×10^4 cm²V⁻¹s⁻¹ which is higher than most 2D semiconductors of similar band gap [47–56] [Fig. 1(e)], suggest their strong potential in electronics

and optoelectronics applications [46]. The broken inversion symmetry of NbOXY generates both in-plane and out-of-plane response – an uncommon but much sought-after behavior in 2D materials [4, 31]. Intriguingly, the orthorhombic crystal of MbOXY generates an additional d_{32} response not commonly found in other 2D materials [see Fig. 1(f) for schematic illustrations of d_{11} , d_{31} and d_{32} piezoelectric responses]. The simultaneously sizable d_{11} and d_{32} responses [see Fig. 1(g) for a comparison with other 2D piezoelectric materials] suggests that NbOXY is an uncommon 2D semiconductor capable of operating in both in-plane and out-of-plane device settings, thus greatly expanding their practicality in piezoelectric and piezoelectronic device applications. We propose a device concept of *directional stress sensor* to illustrate how the d_{31} and d_{32} of NbOXY responses can be harnessed for complementary piezoelectric functionality not found in their non-Janus counterpart. G_0W_0 -BSE calculations further reveals the strong optical anisotropic, broadband visible light absorption, and sharp absorption peaks in the deep UV regime which are much stronger than other 2D optical materials [15] [Fig. 1(h)], thus unravelling the capability of NbOXY in solar energy harvesting and UV photonics applications [57]. The high-mobility, broadband visible light absorption, presence of built-in electric fields and band edge energies compatible with photocatalytic water splitting [58] further suggest the enormous potential of NbOXY for high-efficiency solar-to-hydrogen conversion. Our findings unveil NbOXY as a compelling multifunctional semiconductor family with promising potential in high-performance flexible electronics, optoelectronics, photonics, sensing and sustainable energy harvesting applications.

II. COMPUTATIONAL METHODS

A. Structural Relaxation, Electronic Structures and Transport Properties

First-principles density functional theory (DFT) [59] calculations are performed using the projector-augmented wave method as implemented in the Vienna ab initio simulation package (VASP) [60–62]. We consider the generalized gradient approximation of Perdew, Burke and Ernzerhof (GGA-PBE) as the exchange-correlation functional [63]. For band structure calculations, we employ the range-separated HSE06 hybrid functionals [64, 65]. An energy cut-off of 500 eV, total energy convergence criterion of 10^{-8} eV and a force convergence criteria of less than 10^{-3} eV/Å on each atom are adopted. A vacuum region of > 30 Å along the z direction is added to avoid interactions between two neighboring images Γ -centered k -point meshes of $25 \times 13 \times 1$ in the first Brillouin zone is employed to yield well-converged results, i.e. a and b lattice constant, for the unit cells of the Janus monolayers. VASPKIT is used for postprocessing of the DFT calculation data [66]. Bader charge analysis

is performed to obtain the net charge transfer between the atoms [67].

The carrier mobility is calculated based on the deformation potential theory of Bardeen and Shockley [68],

$$\mu_i^{(\nu)} = \frac{e\hbar^3 C_{2D,i}}{k_B T m_i^{(\nu)} m_d^{(\nu)} E_{l,i}^{(\nu)2}} \quad (1)$$

where the superscript $\nu = e, h$ denotes electron and hole, the subscript $i = x, y$ denotes the two orthogonal directions, $m_i^{(\nu)} = \hbar^2 (\partial^2 \varepsilon_{\mathbf{k}} / \partial k_i^2)$ is the effective mass of ν carrier, $\varepsilon_{\mathbf{k}}$ is the energy dispersion around the band edge assuming a parabolic dispersion relation, $\mathbf{k} = (k_x, k_y)$ is the 2D wave vector, $m_d^{(\nu)} = \sqrt{m_x^{(\nu)} m_y^{(\nu)}}$ is the density of states effective mass of ν carrier, T is the temperature, $C_{2D,i}$ is the 2D elastic modulus along i direction and $E_{l,i}^{(\nu)}$ is the deformation potential constant [69].

B. Thermal, Dynamical, Mechanical and Piezoelectric Properties Calculations

To assess the dynamical stability of NbOXY monolayers, we calculate the phonon frequencies using density functional perturbation theory (DFPT) calculations [70] through the direct supercell method with the $4 \times 2 \times 1$ supercell. The lattice vector is greater than 15 Å as implemented in the Phonopy code [71]. The phonon dispersion at different q points are obtained by computing the force constants on a sufficiently large supercell and Fourier interpolating the dynamical matrices in the primitive cell. Ab initio molecular dynamics (AIMD) simulations of canonical ensemble (i.e. NVT ensemble) are performed to confirm the thermal stability of NbOXY monolayer at 300 K, for 5 ps with a time step of 1 fs, in a $4 \times 2 \times 1$ supercell configuration. The Nose algorithm is used to control the temperature [72]. The piezoelectric effect is determined by third-rank tensors e_{ijk} and d_{ijk} . In the contracted Voigt notation, e_{ijk} and d_{ijk} are reduced to e_{il} and d_{il} , respectively, where $i, j, k = 1, 2, 3$ denotes the three orthogonal spatial directions, and $l = 1, 2, \dots, 6$. The elastic stiffness coefficients (C_{ij}^{3D}) are calculated using the finite difference method [73] and the piezoelectric stress tensors (e_{ij}) are obtained from DFPT in VASP [70], via the following definitions [30, 74],

$$\hat{e}_{ijk} = \frac{\partial P_i}{\partial \varepsilon_{jk}} = \frac{\partial \sigma_{jk}}{\partial E_i}, \quad (2a)$$

$$\hat{d}_{ijk} = \frac{\partial P_i}{\partial \sigma_{jk}} = \frac{\partial \varepsilon_{jk}}{\partial E_i}, \quad (2b)$$

where σ_{jk} , ε_{jk} , P_i and E_i are the stress, strain, intrinsic polarization tensors, and macroscopic electric fields, respectively. The piezoelectric strain coefficient, d_{il} , can then be determined from $e_{il} = \sum d_{ik} C_{kl}$. For monolayers, the 2D elastic coefficients C_{ij} and the piezoelectric

TABLE I. **Summary of DFT calculation data of NbOXY.** Lattice constants a and b , monolayer thickness t , band gap E_g , ionization (VBM) energy of the face with X atoms $E_{ip}^{(X)}$ and with Y atoms $E_{ip}^{(Y)}$, electron affinity (CBM) energy of the surface with X halogen atoms $E_{ea}^{(X)}$ and with Y halogen atoms $E_{ea}^{(Y)}$, built-in dipole potential ΔV , charge transfer from Nb atoms to X halogen atoms $\Delta_{\text{Nb} \rightarrow X}$ and to Y halogen atoms to X halogen atoms $\Delta_{\text{Nb} \rightarrow Y}$, and the charge differences between the X and Y halogen atoms are listed here.

Monolayer	a (Å)	b (Å)	t (Å)	E_g (eV)	$E_{ip}^{(X)}$ (eV)	$E_{ip}^{(Y)}$ (eV)	$E_{ea}^{(X)}$ (eV)	$E_{ip}^{(Y)}$ (eV)	ΔV (eV)	$\Delta_{\text{Nb} \rightarrow X}$ (e)	$\Delta_{\text{Nb} \rightarrow Y}$ (e)	$\Delta_{X/Y}$ (e)
NbOI ₂	3.97	7.59	4.60	1.87	-6.00	-6.00	-4.14	-4.14	0.00	0.72	0.72	0.00
NbOClBr	3.96	6.94	4.07	1.98	-6.86	-6.42	-4.88	-4.44	0.44	1.09	0.91	0.17
NbOClI	3.96	7.23	4.25	1.89	-6.87	-5.83	-4.98	-3.94	1.04	1.10	0.70	0.41
NbOBrI	3.96	7.36	4.41	1.91	-6.53	-5.91	-4.62	-4.00	0.62	0.94	0.70	0.24

stress coefficients e_{ij} are normalized by the slab thickness of the simulation cell along the z direction (L_z) via $C_{ij} = L_z C_{ij}^{3D}$ and $e_{ij} = L_z e_{ij}^{3D}$, where C_{ij}^{3D} and e_{ij}^{3D} are the 3D elastic stiffness and piezoelectric stress coefficients, respectively. Unlike NbOI₂ ($mm2$ point group symmetry), NbOXY structures only have m point group symmetry. Consider only the in-plane strain and stress for 2D systems [30, 74–76], we obtain,

$$\mathbf{e}^{(2D)} = \begin{pmatrix} e_{11} & e_{12} & 0 \\ 0 & 0 & e_{23} \\ e_{31} & e_{32} & 0 \end{pmatrix}, \quad (3a)$$

$$\mathbf{C}^{(2D)} = \begin{pmatrix} C_{11} & C_{12} & 0 \\ C_{12} & C_{22} & 0 \\ 0 & 0 & C_{33} \end{pmatrix}, \quad (3b)$$

$$\mathbf{d}^{(2D)} = \begin{pmatrix} d_{11} & d_{12} & 0 \\ 0 & 0 & d_{23} \\ d_{31} & d_{32} & 0 \end{pmatrix}. \quad (3c)$$

where $d_{11} \neq d_{12}$ and $d_{31} \neq d_{32}$ represent two distinctive in-plane and out-of-plane piezoelectric responses, respectively, and d_{23} is a shear piezoelectric response. The elastic properties (i.e. Young's modulus and Poisson's ratio) are averaged by the Voigt-Reuss-Hill schemes [77] and evaluated using the ElasticPOST code (<https://github.com/hitliaomq/ElasticPOST>) [78–80].

C. Optical Properties Calculations

For the optical properties, random phase approximation (RPA) [81, 82] with G_0W_0 are employed with $6 \times 6 \times 1$ k -point mesh, 300 eV cutoff energy, and the number of bands was tripled. Beyond the RPA approach which considers only the dipole transition, single-shot G_0W_0 approximation [83] is used with the Bethe-Salpeter equation (BSE) [84, 85] within the Tamm-Dancoff approximation which captures the electron-hole interactions. The complex dielectric function $\varepsilon(\omega) = \varepsilon_1(\omega) + i\varepsilon_2(\omega)$ are computed by considering the electromagnetic wave polarization along both x and y directions. The optical

absorption coefficient is obtained as [15],

$$\alpha(\omega) = \frac{\text{Re}[\tilde{\sigma}(\omega)]}{\left|1 + \frac{\tilde{\sigma}(\omega)}{2}\right|^2} \quad (4)$$

where $\tilde{\sigma}(\omega) \equiv \sigma_{2D}(\omega)/\varepsilon_0 c$, $\sigma_{2D}(\omega) = i\varepsilon_0 \omega L_z [1 - \varepsilon(\omega)]$ is the frequency-dependent complex optical conductivity of a 2D system, ε_0 is the permittivity of free space, c is the speed of light, and L_z is the slab thickness of the simulation supercell.

III. RESULTS AND DISCUSSIONS

A. Structural Properties and Monolayer Stability

The lattice structure of NbOXY takes an orthorhombic form with a rectangular network lattice [Fig. 1(a) to (d)]. The Janus nature of NbOXY arises from the two outer sublayers of nonequivalent halogen atoms ($X \neq Y$) sandwiching the central Nb atoms. The rectangular lattice are highly anisotropic with x and y directions composed of O-Nb-O and X-Nb-Y networks, respectively. The lattice constants of the fully relaxed NbOXY are 6.93 Å, 7.22 Å, and 7.36 Å, respectively, along the a -axis (x direction), and about 3.96 Å along the b -axis (y direction) for all Janus monolayers (see Table I for a summary of DFT calculation data). The monolayer thicknesses (t) are 4.067 Å, 4.250 Å and 4.409 Å for NbOClBr, NbOClI, and NbOBrI, respectively, which are comparable to that of the NbOI₂ (4.405 Å).

We examine the (i) dynamical stability; (ii) thermal stability; and (iii) mechanical stability of Janus NbOXY via phonon spectra calculation, AIMD simulations and elastic coefficients analysis based on the Born-Huang criteria [86], respectively (Fig. 2). As shown in Fig. 2(a), the absence of significant soft modes in the phonon spectra confirms the dynamical stability of NbOXY in the freestanding form. The AIMD simulations of NbOXY reveals minute energy fluctuation less than 2 meV after 5 ps at 300 K, with only minimal lattice distortion [Figs. 2(b) and 2(c)], thus confirming the thermal stability of NbOXY at room temperature [87]. To achieve mechanical stability, the Born-Huang criteria requires the elastic coefficients to fulfill the inequalities [86],

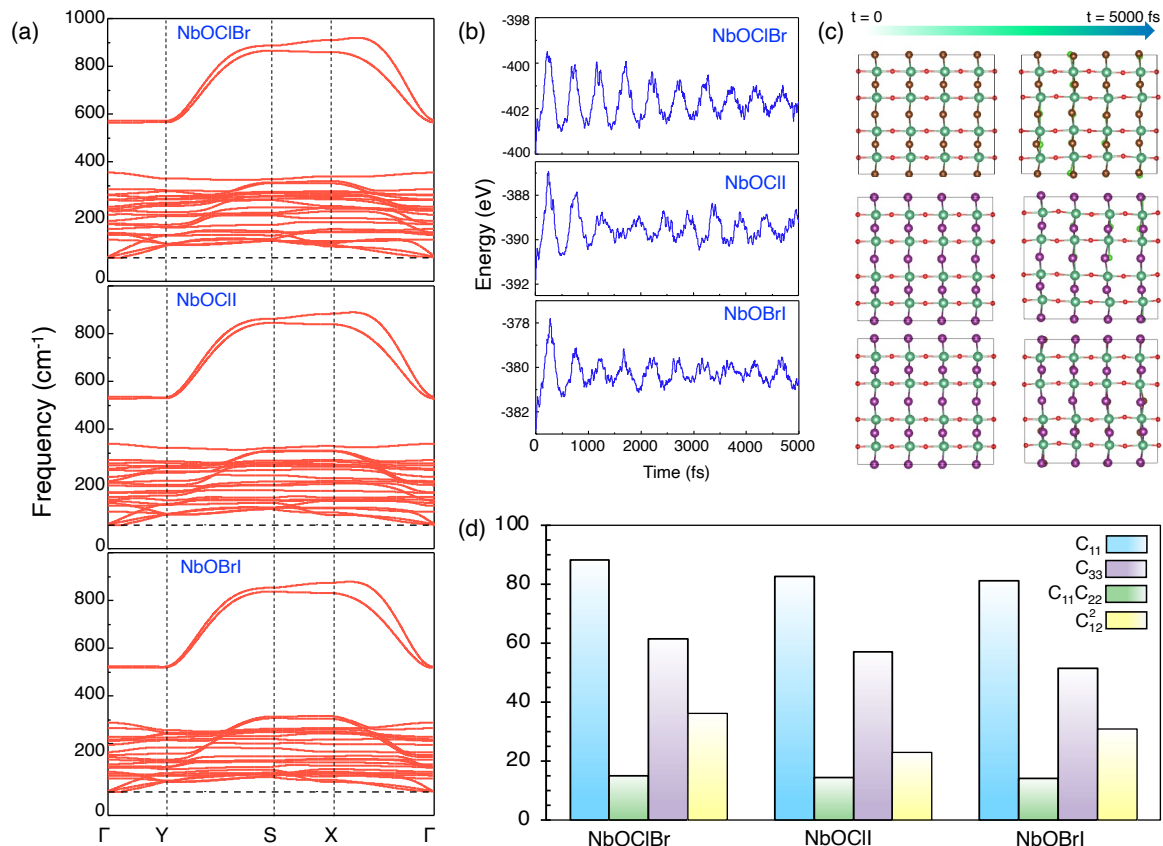


FIG. 2. **Dynamical, thermal and mechanical stability of NbOXY monolayers.** (a) Phonon spectra of the monolayers reveal the absence of significant soft modes around the Γ point; (b) Ad initio molecular dynamics (AIMD) simulations of NbOXY monolayers for a duration of 5000 fs at 300 K. The energy of the 2D systems fluctuate less than 2 meV; (c) Lattice structure of the NbOXY after 5000 ps showing minimal distortions; (d) the elastic coefficients of C_{11} , C_{33} , $C_{11}C_{22}$ and C_{12}^2 of NbOXY fulfil the Born-Huang criteria [86] of $C_{11} > 0$, $C_{33} > 0$ and $C_{11}C_{22} > C_{12}^2$. The C_{11} and C_{33} are in the unit of N/m while $C_{11}C_{22}$ and C_{12}^2 are in the units of $10^2 \text{ N}^2/\text{m}^2$ and N^2/m^2 , respectively.

$C_{11} > 0$, $C_{33} > 0$, and $C_{11}C_{22} > C_{12}^2$. All three NbOXY monolayers fulfil the Born-Huang criteria [Fig. 2(d)]. The predicted NbOXY monolayers are thus dynamically, thermally and mechanically stable. We further note that Janus and non-Janus NbOXY composed of fluorine atoms exhibit significant soft modes (see [Supplementary Materials](#)), and are thus excluded in this study.

B. Electronic structures and electrical properties

1. Electronic Band structures

The band structures and projected density of states (PDOS) of NbOI₂ and NbOXY calculated via HSE06 method are shown in Fig. 3(a). The band gap is 1.98, 1.89 and 1.90 eV for NbOClBr, NbOCII and NbOBrI, respectively, which are comparable to that of NbOI₂ (1.87 eV) [41]. Around the CBM, the bands disperse more sharply along the x direction (i.e. $\Gamma \rightarrow X$) the dispersion around the y direction (i.e. $\Gamma \rightarrow Y_+$ and $\Gamma \rightarrow Y_-$) are relatively flatter, which leads to sharply contrasting trans-

port behaviors along these two orthogonal directions. For non-Janus NbOX₂, the electronic states around the conduction band minima (CBM) valance band maxima (VBM) are predominantly from the Nb atoms whereas the VBM also has a sizable contribution from the halogen atoms [see PDOS in Fig. 3(a)] [41]. Janus NbOXY has a similar electronics structures with CBM and VBM states being dominated by the Nb atoms. However, the VBM has a significantly lower contributions from the halogen atoms [see PDOS in Figs. 3(a)].

2. Band alignment, interface potential difference and overall photocatalytic water splitting

The CBM and VBM energies of NbOI₂ and NbOXY are shown in Fig. 3(b). Interestingly, the CBM (VBM) of NbOI₂ is higher (lower) than the water reduction (oxidation) potential of $E_{\text{H}^+/\text{H}_2} = -4.44 \text{ eV}$ ($E_{\text{O}^-/\text{H}_2\text{O}} = -5.67 \text{ eV}$) [88, 89] for hydrogen (oxygen) molecule production, thus suggesting the potential of NbOI₂ in photocatalytic overall water splitting application [90]. Due

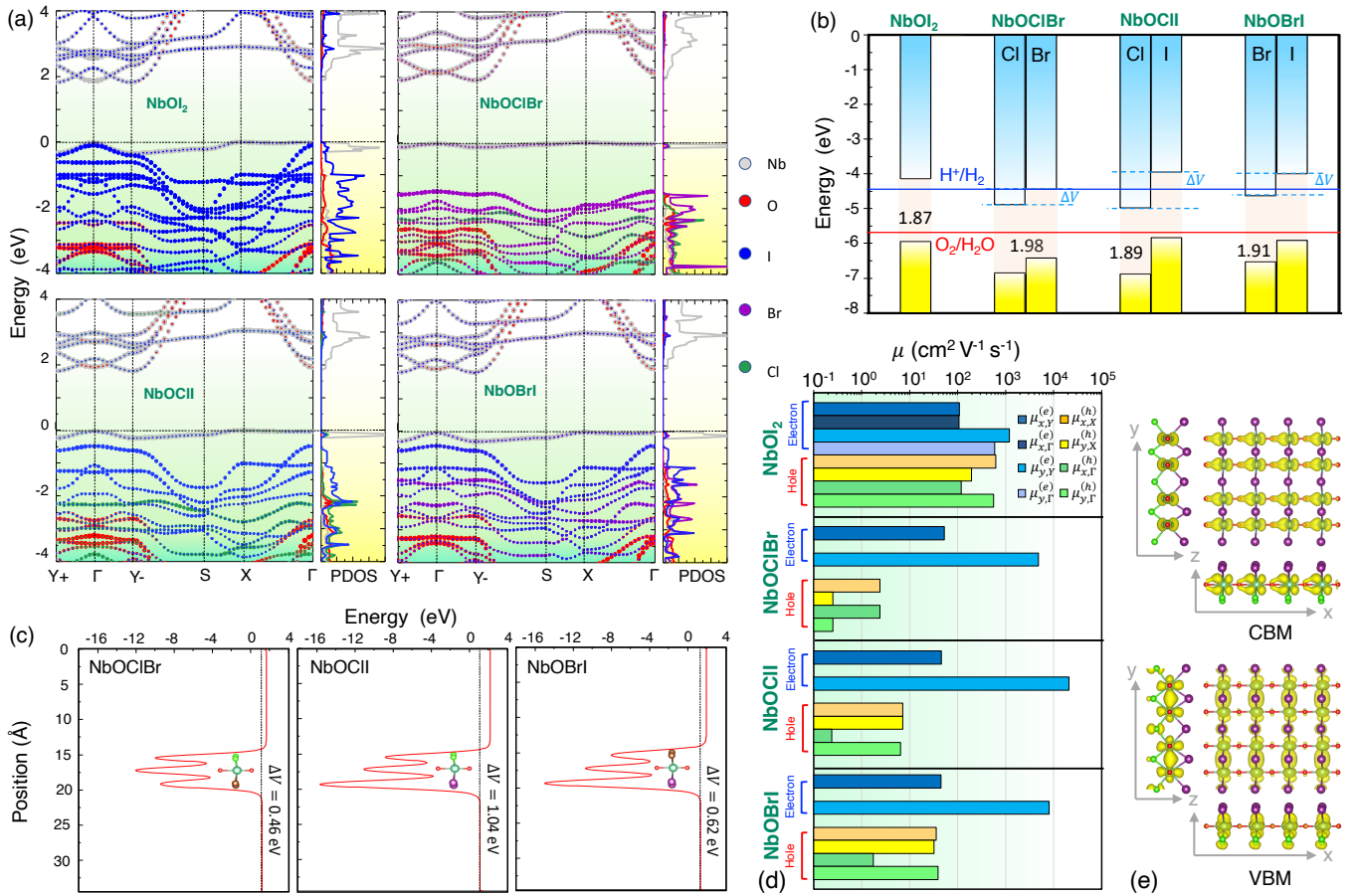


FIG. 3. **Electronic structures of NbOXY.** (a) Band structures. (b) The conduction and valence band alignments of NbOI₂ and NbOXY. The X and Y surface exhibits an offset of ΔV in Janus NbOXY. All values are in the unit of eV. (c) Plane-averaged electrostatic potential plot. (d) Anisotropic electron and hole mobilities of NbOXY. (e) The wave function distribution of the CBM and VBM states of NbOCII monolayer.

to the inversion symmetry breaking of Janus NbOXY, unequal charge transfer to the X and Y halogen atoms [see Table I for a summary for the Bader charge analysis] leads to a built-in intrinsic electric field along the out-of-direction of the lattice [91, 92]. Correspondingly, a sizable interface potential difference (ΔV) arises across the two surfaces of NbOXY, causing the CBM and VBM to offset by ΔV on the X and Y planar surface as illustrated in the band alignment diagram in Fig. 3(b) as well as the plane-averaged electrostatic potential profile in Fig. 3(c). Here ΔV signifies a work function difference on the two opposite planar surface of NbOXY and is directly proportional to the charge transfer difference between Nb \rightarrow X and Nb \rightarrow Y (see [Supplementary Materials](#)). While NbOCIBr is incompatible for hydrogen evolution reaction (HER) due to the close proximity of the CBM to $E_{\text{H}^+/\text{H}_2}$, NbOCII and NbOBrI are compatible with both HER and oxygen evolution reaction (OER) with sizable energy differences, $\Delta E_1 \equiv E_{\text{CBM}} - E_{\text{H}^+/\text{H}_2}$ and $\Delta E_2 \equiv E_{\text{O}_2/\text{H}_2\text{O}} - E_{\text{VBM}}$, which are critically needed for enhancing the HER and OER activities [88]. The $(\Delta E_1, \Delta E_2)$ of NbOCII and NbOBrI are (0.50, 1.20) eV and (0.44, 0.86)

eV, respectively, which significantly outperforms that of the non-Janus NbOI₂, i.e. $(\Delta E_1, \Delta E_2) = (0.30, 0.28)$ eV. In addition, the presence of a built-in electric field in NbOXY enables the efficient spatial separation of photoexcited electron-hole pairs onto the two opposite surface [89], with electron (hole) preferentially migrates towards the surface with X (Y) halogen atoms upon photoexcitation. Importantly, the combined factors of (i) sizable $(\Delta E_1, \Delta E_2)$ that is beneficial for enhancing HER and OER activities; (ii) built-in electric field that is beneficial for photoexcited electron-hole pair separation; (iii) strong optical absorption covering visible and ultraviolet regimes that is beneficial for optimal coverage of solar spectrum (discussed below); and (iv) large carrier mobility reaching well over 10^4 cm²V⁻¹s⁻¹ (discussed below), suggest the capability of NbOXY monolayers in photocatalytic water splitting applications [93, 94].

TABLE II. **Electrical transport properties of NbOI₂ and NbOXY.** The effective masses, $m_i^{(\nu)}$, are in the unit of m_0 where m_0 is free electron mass. The deformation potential constants, $E_{l,i}^{(\nu)}$, are in the unit of eV. The elastic moduli, $C_{2D,i}$, are in the unit of Jm⁻². The carrier mobilities, $\mu_i^{(\nu)}$, are in the unit of cm²V⁻¹s⁻¹. The band edge position, i.e. Γ , Y_{\pm} and X , are marked directly after the numeric values as superscript for simplicity.

Material	$m_x^{(e)}$	$m_y^{(e)}$	$m_x^{(h)}$	$m_y^{(h)}$	$E_{l,x}^{(e)}$	$E_{l,y}^{(e)}$	$E_{l,x}^{(h)}$	$E_{l,y}^{(h)}$	$C_{2D,x}$	$C_{2D,y}$	$\mu_x^{(e)}$	$\mu_y^{(e)}$	$\mu_x^{(h)}$	$\mu_y^{(h)}$
NbOI ₂	0.916 ^{Y\pm}	0.797 ^{Y\pm}	8.082 ^X	1.219 ^X	4.40 ^{Y\pm}	1.81 ^{Y\pm}	0.32 ^X	1.33 ^X	75.61	61.87	106.609 ^{Y\pm}	593.647 ^{Y\pm}	621.010 ^X	195.035 ^X
	0.334 ^{Γ}	0.622 ^{Γ}	33.688 ^{Γ}	0.782 ^{Γ}	9.85 ^{Γ}	1.97 ^{Γ}	0.28 ^{Γ}	0.76 ^{Γ}			109.217 ^{Γ}	1199.744 ^{Γ}	119.213 ^{Γ}	563.216 ^{Γ}
NbOCIBr	0.500 ^{Y\pm}	1.370 ^{Y\pm}	13.010 ^X	30.540 ^X	9.50 ^{Y\pm}	0.50 ^{Y\pm}	1.78 ^X	2.99 ^X	92.31	64.26	52.733 ^{Y\pm}	4836.536 ^{Y\pm}	2.397 ^X	0.252 ^X
			168.440 ^{Γ}	29.218 ^{Γ}			1.87 ^{Γ}	3.67 ^{Γ}					0.048 ^{Γ}	0.050 ^{Γ}
NbOCII	0.578 ^{Y\pm}	1.090 ^{Y\pm}	11.395 ^X	6.095 ^X	9.30 ^{Y\pm}	0.28 ^{Y\pm}	1.64 ^X	1.96 ^X	85.83	66.41	46.150 ^{Y\pm}	20888.791 ^{Y\pm}	7.170 ^X	7.261 ^X
			128.701 ^{Γ}	0.28 ^{Γ}			1.79 ^{Γ}	2.12 ^{Γ}					0.240 ^{Γ}	6.457 ^{Γ}
NbOBrI	0.614 ^{Y\pm}	1.014 ^{Y\pm}	9.989 ^X	2.410 ^X	9.01 ^{Y\pm}	0.46 ^{Y\pm}	1.00 ^X	1.88 ^X	83.17	63.40	45.118 ^{Y\pm}	8094.971 ^{Y\pm}	36.206 ^X	32.366 ^X
			71.119 ^{Γ}	1.380 ^{Γ}			1.19 ^{Γ}	1.59 ^{Γ}					1.770 ^{Γ}	39.153 ^{Γ}

3. Transport properties

The electrical mobilities of NbOI₂ and NbOXY are calculated at room temperature ($T = 300$ K). [see Fig. 3(d) and Table II]. From the deformation potential theory of Bardeen and Shockley [68] in Eq. (1), the electrical mobility follows the proportionality, $\mu_i^{(\nu)} \propto C_{2D,i}/m_i^{(\nu)-3/2}E_{l,i}^{(\nu)-2}$. As μ has a second order dependence on E_l , which is sensitively influenced by the wave function distribution of the band edge states, the spatial extend of the band edge states thus play an important role in governing carrier transport. We first consider electron mobility in the conduction band. For NbOI₂, as the conduction band edge at the Γ and the Y_{\pm} points are separated by only about 26 meV, both *valleys* are expected to contribute to the electron conduction current. The electron mobilities of both valleys are calculated, i.e. $\mu_{i,Y_{\pm}}^{(e)}$ and $\mu_{i,\Gamma}^{(e)}$, respectively, where $i = x, y$ represents the two orthogonal crystal directions. In contrast, the Γ valley in NbOXY is energetically well-separated from the actual CBM at Y_{\pm} valley by a substantial energy, we thus consider only $\mu_{i,Y_{\pm}}^{(e)}$ for NbOXY. The electron mobility is highly anisotropic in both NbOX₂ and NbOXY with $\mu_{x,Y_{\pm}/\Gamma}^{(e)} \ll \mu_{y,Y_{\pm}/\Gamma}^{(e)}$ [Fig. 3(d)]. The larger electron mobility in the y direction ($\mu_{y,Y_{\pm}/\Gamma}^{(e)}$) is a direct consequence of the weak orbital overlap along the y crystal direction [see the band-decomposed charge density distributions of the CBM states of NbOCII as a representative example in Fig. 3(e)]. Lattice distortion along the y direction does not generate significant CBM energy shifting, thus resulting in small $E_{l,y}^{(\text{CBM})}$. Since $\mu_y^{(e)} \propto \left(E_{l,y}^{(\text{CBM})}\right)^{-2}$, the electron mobility is significantly enhanced, yielding high mobility values of $\mu_{y,Y_{\pm}/\Gamma}^{(e)} = 10^3 \sim 10^4 \times 10^4$ cm²V⁻¹s⁻¹ in NbOXY. Particularly, NbOCII has an exceedingly large mobility $\mu_{y,Y_{\pm}}^{(e)} = 2 \times 10^4$ cm²V⁻¹s⁻¹, which is considerably higher than the vast majority of 2D semiconductors with band gap $E_g \gtrsim 2$ eV.

For the hole conduction in valance bands, because of

the close energetic proximity of the Γ point and the CBM at X point with minute energy separation ~ 40 meV, we calculate the hole mobility at both X and Γ point, i.e. $\mu_{i,X}^{(h)}$ and $\mu_{i,\Gamma}^{(h)}$, for all monolayers. Interestingly, the wave function distribution of the VBM states is contrary to that of the CBM states, i.e. strong orbital overlap strongly (weakly) along the x (y) crystal direction [see Fig. 3(e)]. However, for hole conduction at the X point of NbOCII and NbOBrI, the anisotropy of $E_{l,x} < E_{l,y}$ is *compensated* by a sizable hole effective mass anisotropy of $m_x^{(h)} > m_y^{(h)}$. Their hole mobilities are thus comparable or approximately isotropic at the X points, i.e. $\mu_{x,X}^{(h)} \approx \mu_{x,\Gamma}^{(h)}$. At the Γ point of NbOCII and NbOBrI, the anisotropy of $E_{l,x} < E_{l,y}$ is insufficient to negate the exceedingly large hole effective mass of $m_x^{(h)} \gg m_y^{(h)}$. An unexpected mobility anisotropy of $\mu_{x,\Gamma}^{(h)} \ll \mu_{y,\Gamma}^{(h)}$ thus occurs despite the weak orbital overlap along the x crystal direction.

It should be noted that the electron mobility anisotropy $\mu_{x,Y_{\pm}/\Gamma}^{(e)} < \mu_{y,Y_{\pm}/\Gamma}^{(e)}$ and the hole conduction anisotropy at Γ point $\mu_{x,\Gamma}^{(h)} < \mu_{y,\Gamma}^{(h)}$ originate from completely different mechanisms: (i) $\mu_{x,\Gamma}^{(h)} < \mu_{y,\Gamma}^{(h)}$ is caused by the extraordinarily strong hole effective mass anisotropy; (ii) whereas $\mu_{x,Y_{\pm}/\Gamma}^{(e)} < \mu_{y,Y_{\pm}/\Gamma}^{(e)}$ arises from the nearly absent y -directional wave function overlap of the CBM states. We further note that, hole transport in NbOCIBr is distinctive from the other NbOXY monolayers. NbOCIBr exhibits $\mu_{x,X/\Gamma}^{(h)} > \mu_{y,X/\Gamma}^{(h)}$ at both X and Γ points due to the distinctive hole effective mass anisotropy: (i) $m_x^{(h)} < m_y^{(h)}$ at the X point and $E_{l,x}^{(h)} < E_{l,y}^{(h)}$ jointly enhances x -directional hole mobility, leading to $\mu_{x,X}^{(h)} > \mu_{y,X}^{(h)}$; whereas (ii) the milder (and opposite) effective mass anisotropy of $m_x^{(h)} > m_y^{(h)}$ at the Γ point is insufficient to negate the $E_{l,x}^{(h)} < E_{l,y}^{(h)}$ that amplifies x -directional transport, thus leading to $\mu_{x,\Gamma}^{(h)} > \mu_{y,\Gamma}^{(h)}$ which is akin to the case of X point.

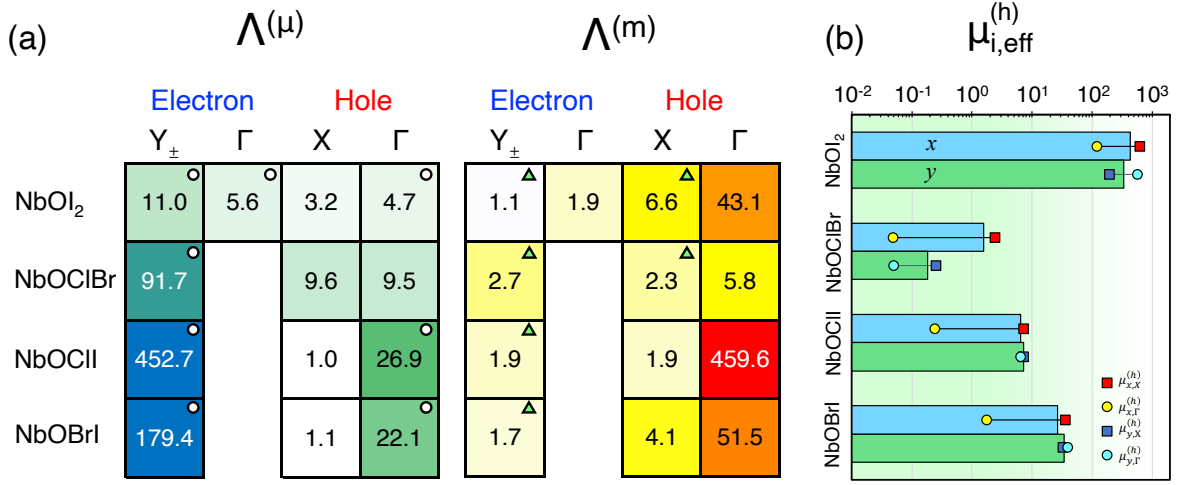


FIG. 4. **Transport anisotropy and effective hole mobility.** (a) shows the electrical mobility ratios and effective mass ratios at different conduction and valance band valleys. The circle and triangle symbols denote $\mu_x^{(\nu)} < \mu_y^{(\nu)}$ and $m_x^{(\nu)} < m_y^{(\nu)}$, respectively. Otherwise, $\mu_x^{(\nu)} > \mu_y^{(\nu)}$ and $m_x^{(\nu)} > m_y^{(\nu)}$. (b) Effective hole mobility of multi-valley hole transport in NbOI₂ and NbOXY. Blue and green bars denote x - and y -directional hole effective mobility, respectively.

4. Transport anisotropy and effective mobility

We summarize the mobility and effective mass anisotropy in Fig. 4(a) where the anisotropy ratios are defined as,

$$\Lambda(\mu) \equiv \frac{\max[\mu_x^{(\nu)}, \mu_y^{(\nu)}]}{\min[\mu_x^{(\nu)}, \mu_y^{(\nu)}]}, \quad (5a)$$

$$\Lambda(m) \equiv \frac{\max[m_x^{(\nu)}, m_y^{(\nu)}]}{\min[m_x^{(\nu)}, m_y^{(\nu)}]}, \quad (5b)$$

$\max[\dots]$ and $\min[\dots]$ are the maximum and minimum functions, respectively. The electron mobility of NbOXY exhibits the enormous mobility anisotropy in the order of 10² whereas the Γ -point hole effective mass exhibits strong anisotropy in the order of 10 ~ 10². Such exceptionally anisotropic transport properties of NbOXY suggests new avenues for nanoelectronics device engineering in which the carrier mobility can be tuned over two orders of magnitude by selectively aligning the electrodes along different crystal directions.

The presence of multiple valance band valleys in NbOXY can co-contribute to hole conduction current. However, the electrical current from different valleys cannot be directly distinguished from typical transport measurement. It is thus important to determine the *effective hole mobility* of the total transport current that includes the current conduction in multiple valleys [95, 96]. We consider a drift current transport picture in which the total hole current density is given by

$$\mathcal{J}_{i,\Gamma}^{(h)} = en_{\Gamma}^{(h)} \mu_{i,\text{eff}}^{(h)} \mathcal{E}, \quad (6)$$

where \mathcal{E} is the applied electric field along the $i = x, y$ direction, $\mu_{i,\text{eff}}^{(h)}$ is the effective hole mobility inclusive of both X and Γ valleys, and $n_{\Gamma}^{(h)} = n_X^{(h)} + n_{\Gamma}^{(h)}$ is the *total* 2D carrier density inclusive of both X and Γ valleys, i.e. $n_X^{(h)}$ and $n_{\Gamma}^{(h)}$, respectively. Since the total hole current density is contributed by both valleys, we can equivalently write

$$\mathcal{J}_{i,\Gamma}^{(h)} = \mathcal{J}_{i,X}^{(h)} + \mathcal{J}_{i,\Gamma}^{(h)}, \quad (7)$$

where $\mathcal{J}_{i,X}^{(h)} = en_X^{(h)} \mu_{i,X}^{(h)} \mathcal{E}$ and $\mathcal{J}_{i,\Gamma}^{(h)} = en_{\Gamma}^{(h)} \mu_{i,\Gamma}^{(h)} \mathcal{E}$ are the X and Γ valley current component, respectively. The 2D carrier densities are

$$n_{\lambda}^{(h)} = \frac{2}{(2\pi)^2} \int_{-\infty}^{-\varepsilon_{\lambda}} dk_x dk_y [1 - f(\varepsilon_{\mathbf{k}}, \varepsilon_F, T)], \quad (8)$$

where $\lambda = X, \Gamma$ denotes the band edge position, $f(\varepsilon_{\mathbf{k}}, \varepsilon_F, T)$ is the Fermi-Dirac distribution function and ε_F is the Fermi level. Consider the non-degenerate regime with ε_F several times larger than $k_B T$ which is well achievable at room temperature, the Fermi-Dirac distribution function reduces to the semiclassical limit of $f(\varepsilon_{\mathbf{k}}, \varepsilon_F, T) \approx \exp[-(\varepsilon_{\mathbf{k}} - \varepsilon_F)/k_B T]$. Equations (6) to (8) can be combined to yield

$$\mu_{i,\text{eff}}^{(h)} = \frac{\mu_{i,X}^{(h)}}{1 + \frac{n_{\Gamma}^{(h)}}{n_X^{(h)}}} \left(1 + \frac{n_{\Gamma}^{(h)} \mu_{i,\Gamma}^{(h)}}{n_X^{(h)} \mu_{i,X}^{(h)}} \right), \quad (9)$$

where the hole density ratio is

$$\frac{n_{\Gamma}^{(h)}}{n_X^{(h)}} = \frac{m_{d,\Gamma}^{(h)}}{m_{d,X}^{(h)}} \exp\left(-\frac{\Delta_{X-\Gamma}}{k_B T}\right), \quad (10)$$

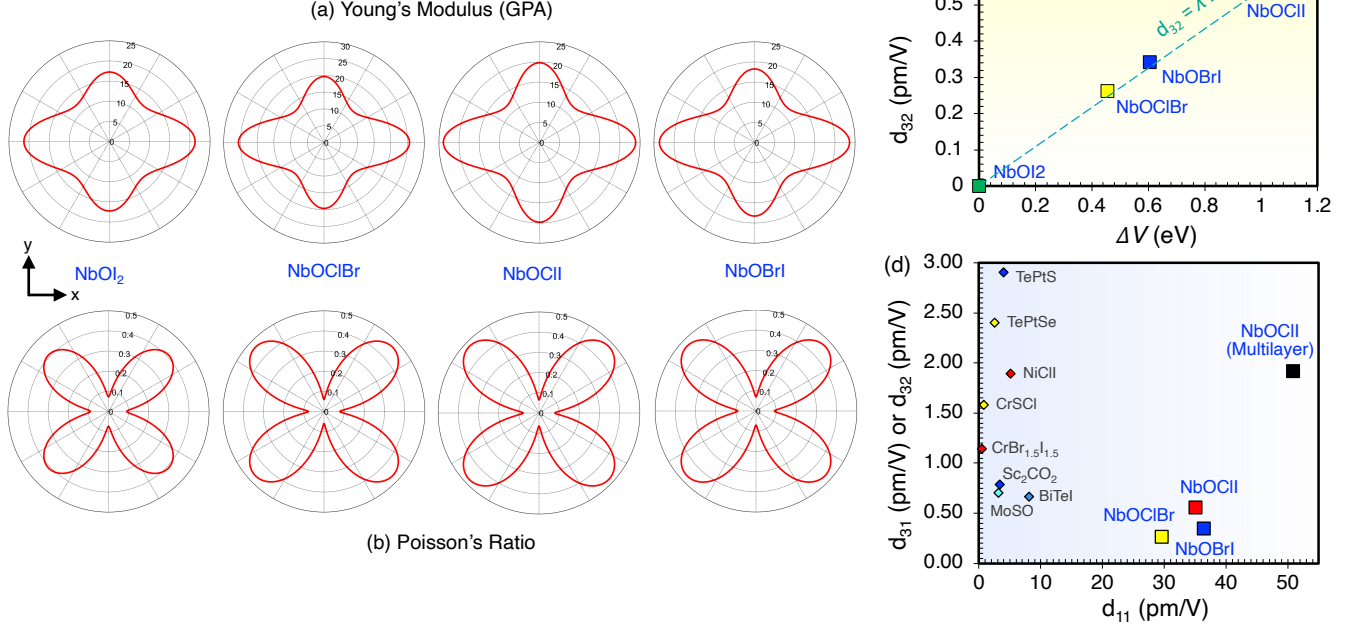


FIG. 5. **Anisotropic elastic properties and out-of-plane piezoelectric response of NbOXY monolayers.** Directional dependence of (a) Young's modulus and (b) Poisson's Ratio. (c) Correlation between d_{32} and work function differences ΔV . The fitting equation $d_{32} = \lambda\Delta V$ has an excellent linear fit with R^2 value of 0.999. (d) Comparison of NbOXY (d_{11} and d_{32}) with other 2D materials of sizable out-of-plane piezoelectricity (i.e. $d_{32} > 0.5$ pm/V). The in-plane and out-of-plane piezoelectric responses of multilayer NbOCII is significantly larger than the monolayer counterpart.

Here $m_{d,\lambda}^{(h)} = \sqrt{m_{x,\lambda}^{(h)} m_{y,\lambda}^{(h)}}$ is the DOS effective mass of hole at the λ point and $\Delta_{X-\Gamma} \equiv |\varepsilon_X - \varepsilon_\Gamma|$ is the energy separation between X and Γ points. The effective hole mobility along the x and y directions are shown in Fig. 4(b). As $\mu_{i,\text{eff}}^{(h)}$ in Eq. (9) is essentially the carrier density-weighted average of $\mu_{i,X}^{(h)}$ and $\mu_{i,\Gamma}^{(h)}$, the effective mobility $\mu_{i,\text{eff}}^{(h)}$ is intermediate between the $\mu_{i,X}^{(h)}$ and $\mu_{i,\Gamma}^{(h)}$. Since $\mu_{i,\text{eff}}^{(h)}$ takes into account the multi-valley transport of holes, we expect $\mu_{i,\text{eff}}^{(h)}$ to exhibit a better agreement with experimental transport measurement when compared with the individual valley mobilities of $\mu_{i,X}^{(h)}$ and $\mu_{i,\Gamma}^{(h)}$. In general, $\mu_{x,\text{eff}}^{(h)} \approx \mu_{y,\text{eff}}^{(h)}$ for NbOI₂, NbOCl and NbOBrI. In contrast, NbOCIBr exhibits a more dramatic hole effective mobility anisotropy due to the effective mass anisotropy of $m_x^{(h)} < m_y^{(h)}$ at X point as discussed above.

C. Mechanical and Piezoelectric Properties

1. Young's modulus and Poisson's ratio

We now examine the Young's modulus and Poisson's ratio of NbOXY (Fig. 5). Table III summarizes the mechanical properties of NbOXY. NbOXY exhibits me-

chanical anisotropy in terms of Young's modulus [Fig. 5(a)]. The Young's modulus peaks along x and y directions, with values lying between 20 GPa and 25 GPa along the x direction, and between 18 GPa and 20 GPa along the y direction. The anisotropy ratio of the Young's modulus is only $\lesssim 2$ for NbOXY, which is less profound when compared to other 2D materials with giant mechanical anisotropy [97, 98]. It is noteworthy that the Young's modulus of NbOXY is significantly smaller than many other 2D materials, such as graphene, boron nitride and TMDC [99], thus suggesting their excellent mechanical flexibility useful for flexible electronics applications. Unlike auxetic 2D materials [100], the Poisson's ratio of NbOXY is entirely positive and exhibits directional dependence with maximum values of ~ 0.45 along the directions 45° to the x and y axis [Fig. 5(b)].

2. Piezoelectric coefficients

The 2D piezoelectric stress coefficients e_{ij} and the piezoelectric strain coefficients d_{ij} are summarized in Table III. In contrast to the centrosymmetric NbOI₂ with $d_{31} = 0$, the broken inversion symmetry in NbOXY generates two distinctive out-of-plane piezoelectric responses, as characterized by d_{31} and d_{32} . Janus NbOXY monolayers retain the large d_{11} of 35.05, 29.62 and 36.49 pm/V for NbOCII, NbOCIBr and NbOBrI, respectively.

TABLE III. **Mechanical and piezoelectric properties of NbOXY.** The piezoelectric stress coefficients e_{ij} in the unit of 10^{-10} C/m, elastic stiffness coefficients C_{ij} in the unit of N/m , and the piezoelectric strain coefficients d_{ij} in the unit of pm/V.

Monolayer	e_{11}	e_{12}	e_{31}	e_{32}	e_{23}	C_{11}	C_{12}	d_{11}	d_{12}	d_{31}	d_{32}	d_{23}
NbOI ₂ ^a	31.60	-1.00	0.00	0.00	0.70	75.60	5.30	42.20	-5.10	0.000	0.00	5.20
NbOI ₂	31.70	-1.11	0.00	0.00	0.71	73.31	4.91	43.60	-5.40	0.000	0.00	5.21
NbOCIBr	25.91	-1.29	0.07	0.19	0.86	88.11	6.01	29.62	-3.90	0.070	0.26	5.80
NbOCII	28.76	-1.28	0.09	0.38	0.90	82.66	4.80	35.05	-4.37	0.074	0.55	6.29
NbOBrI	29.34	-1.22	0.02	0.22	0.75	81.18	5.57	36.49	-5.11	0.002	0.34	5.31

^a DFT calculation data from Ref. [38]

Such d_{11} values are only slightly lower than that of NbOI₂ and outperforms a large number of 2D in-plane piezoelectric materials [Fig. 1(g)]. The out-of-plane d_{31} responses are 0.074, 0.070 and 0.002 pm/V for NbOCII, NbOCIBr and NbOBrI, respectively. The d_{31} of NbOCII and NbOCIBr are more than 2 times larger than that of MoSTe monolayer (0.030 pm/V) – the top performer in the Janus TMDC family [30] – and several other 2D out-of-plane piezoelectric materials [Fig. 1(g)]. In addition, the d_{32} coefficient is several times larger than d_{31} , with 0.26, 0.55 and 0.34 pm/V for NbOCII, NbOCIBr and NbOBrI, respectively. Here NbOCII is a particularly exceptional 2D semiconductor with simultaneously large in-plane (d_{11}) and sizable out-of-plane (d_{32}) piezoelectricity. Interestingly, d_{32} is directly proportional to the interface potential difference ΔV , exhibiting an excellent linear fit (i.e. $R^2 \approx 0.999$) [Fig. 5(c)] which can be captured by a simple semi-empirical expression,

$$d_{32} = \lambda \Delta V, \quad (11)$$

where $\lambda = 0.5421$ pm/eV². Here d_{32} and ΔV are in the units of pm/V and eV, respectively. The linear relationship between out-of-plane piezoelectricity in 2D Janus materials and ΔV has not been reported previously. Such linear relationship suggests the importance of having a strong built-in dipole potential in order to achieve strong d_{32} responses. It should be noted that although other 2D piezoelectric materials have been predicted to exhibit out-of-plane piezoelectric responses stronger than NbOXY, most of these materials have significantly smaller $d_{11} < 10$ pm/V. Figure 5(d) compares NbOXY with other 2D piezoelectric materials with large out-of-plane response, i.e. $d_{31} > 0.5$ pm/V, in terms of their in-plane and out-of-plane piezoelectricity. It can be seen that d_{31} or d_{32} generally decreases with larger d_{11} . Nevertheless, NbOCII still retains a sizable out-of-plane piezoelectricity of $d_{32} = 0.55$ pm/V despite having an exceedingly large $d_{11} = 35.05$ pm/V. We further calculate the piezoelectric coefficients of *multilayer* NbOCII, which yields significantly amplified piezoelectric coefficients of $d_{11} = 50.86$ pm/V, $d_{31} = 1.92$ pm/V and $d_{32} = -1.04$ pm/V, thus suggesting that layer number engineering can be used to effectively enhance both in-plane and out-of-plane piezoelectricity.

D. Optical properties

We now investigate the optical properties of NbOXY. The imaginary part of the dielectric function ε_2 and the absorption coefficients are shown in Figs. 6(a) and 6(b), respectively, calculated using G_0W_0 -RPA and G_0W_0 -BSE methods. The optical properties obtained via the G_0W_0 -RPA method, which omits the important excitonic effects, differ significantly from that of the G_0W_0 -BSE method [101]. Especially in the visible regime, G_0W_0 -RPA severely overestimates the optical absorption of NbOXY. Since G_0W_0 -BSE method exhibit better agreement with experiments [102], we focus our discussion on the G_0W_0 -BSE results in the following.

In general, the optical absorption spectra are highly anisotropic and exhibit strong *linear optical dichroism* between the x and y directions [103]. The optical absorption in the infrared to red-visible regime for x -polarized light is stronger than that for y -polarized light. In contrast, the optical absorption of y -polarized light is stronger than that of x -polarized light in the blue-visible to ultraviolet regime. The nearly-full coverage of the infrared-visible-UV spectral regime by x - and y -directional optical responses thus suggests the potential of NbOXY in solar energy conversion applications, and can complement the conversion efficiency of photocatalytic water splitting in NbOCII and NbOBrI as discussed above.

The strong linear optical dichroism of NbOXY originate from their anisotropic electronic dispersion. The band structure disperses less in the y direction when compared to that in the x direction, thus resulting in an overall stronger optical absorption along the y direction [41]. We quantify the optical anisotropy as [104, 105],

$$\Lambda^{(\text{opt})}(\hbar\omega) = \frac{\max[\alpha_x(\hbar\omega), \alpha_y(\hbar\omega)]}{\min[\alpha_x(\hbar\omega), \alpha_y(\hbar\omega)]}, \quad (12)$$

where $\alpha_{x,y}(\hbar\omega)$ is the absorption coefficient of (x, y) direction, respectively, at photon energy $\hbar\omega$. NbOXY exhibit significant $\Lambda^{(\text{opt})} \sim 10$ in the visible regime (i.e. $\hbar\omega \gtrsim 2$ eV), thus offering an avenue to straightforwardly determine the crystal direction using polarization optical microscope [106]. In the deep UV regime, an exceedingly large $\Lambda^{(\text{opt})} > 10^2$ can be achieved. At around 500 nm (i.e. $\hbar\omega \approx 2.48$ eV), we obtain $\Lambda^{(\text{opt})} = 1.8, 11.3, 5.5$ for

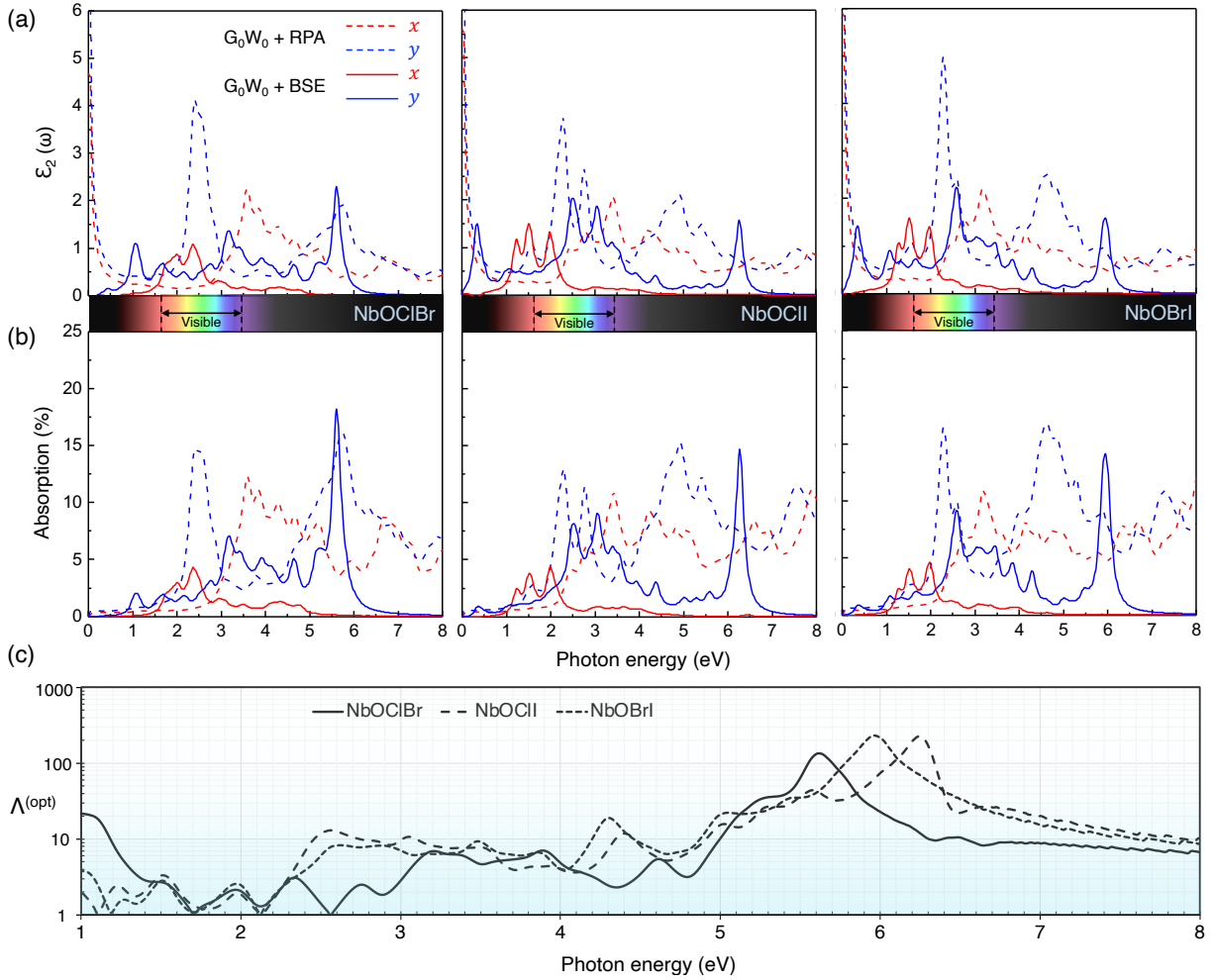


FIG. 6. **Strong optical absorption and linear optical dichroism in NbOXY monolayers.** (a) Imaginary part of the dielectric function. (b) Absorption spectra. (c) Optical anisotropy ratio as a function of photon energy.

NbOClBr, NbOClI, and NbOBrI, respectively, which are comparable or larger than that of NbOI₂ ($\Lambda^{(\text{opt})} = 1.75$) [104], PdSe₂ monolayer ($\Lambda = 1.09$) [107] and GeSe ultra-thin film ($\Lambda = 1.09$) [105]. The anisotropic optical absorption of NbOXY monolayers suggest their potential for polarization-sensitive photonics applications, such as linear polarizers and polarization-dependent photodetectors.

We further note that a remarkably strong optical absorption peak is present at the deep UV regime ($> 5\text{eV}$) for NbOXY monolayers. The peak absorption reaches 18.2 %, 14.7 % and 14.2% for NbOClBr, NbOClI and NbOBrI monolayers, respectively, at the peak frequencies of 5.6 eV, 6.3 eV and 5.9 eV. Such absorption peaks are significantly stronger and ‘deeper’ in the UV regime as compared to the vast majority of previously studied 2D materials [15] [see Fig. 1(h)], thus suggesting the potential of NbOXY for UV photonics and photodetector applications.

E. Proposal of piezoelectric directional stress sensing

Although 2D out-of-plane piezoelectric materials have been extensively studied computationally, how such properties can be harnessed for device applications remain largely unexplored thus far. Here we illustrate how the d_{31} and d_{32} can be harnessed for *directional mechanical stress sensing*. The operation of the proposed device (see Fig. 7 for a schematic illustration) is analogous to an electromagnetic wave polarizer. Consider an incoming incident linearly polarized electromagnetic wave of unknown polarization angle ϕ [see Fig. 7(a)]. The ϕ can be determined straightforwardly using two perpendicularly oriented polarizer which selectively reads out the x and y components of the wave intensity, i.e. I_x and I_y , and hence $\phi = \tan^{-1} I_y/I_x$. Analogously, two NbOXY piezoelectric elements, **A** and **B**, can be stacked onto a flexible substrate with their crystal axis perpendicular to each other [see Fig. 7(b) for the side, back and front views of the proposed device]. Here the elements **A** and

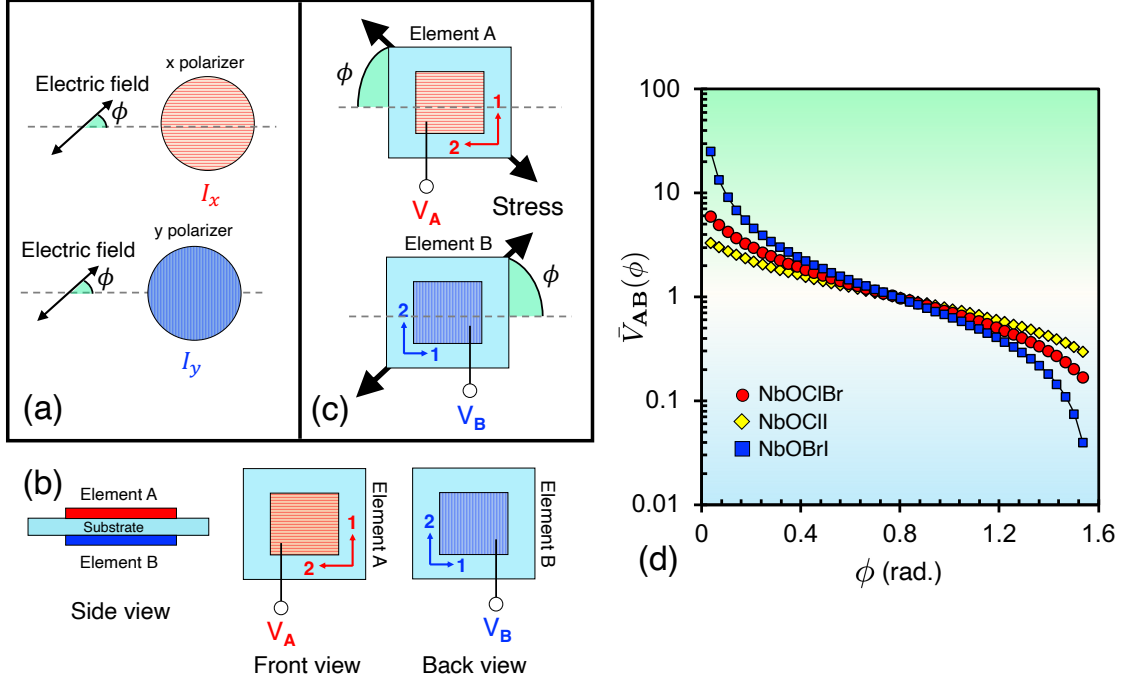


FIG. 7. **Concept of directional stress sensing based on out-of-plane piezoelectricity in NbOXY.** (a) Schematic drawing showing the determination of electromagnetic wave polarization angle ϕ using two polarizer measurements. (b) Schematic drawing of the proposed directional stress sensing devices composed of two back-to-back NbOXY sandwiching a flexible substrate. (c) Directional stress sensing mechanism for a mechanical stress applied at angle of ϕ . (d) $\bar{V}_{AB}(\phi)$ as a function of ϕ shows distinctive value for each ϕ , thus allowing the direction of the mechanical stress to be determined.

B serve the same role as that of the orthogonal polarizers in the electromagnetic analogy. Consider a tensile stress applied purely along the x -direction, the element **A** is mechanically stressed along the ‘2’ axis which produces larger electrical response via d_{32} process, while the element **B** is mechanically stress along the ‘1’ axis with smaller electrical response via d_{31} process. A comparison of these signals generated from **A** and **B** thus allows the direction of the stress to be determined.

More generally, for a mechanical stress applied along the plane of the device, $\mathbf{T} = (T \cos \phi, T \sin \phi)^T$ where T is the magnitude of the stress, ϕ is the angle with respect to the ‘2’ axis of element **A** and \mathcal{T} denotes transpose, the displacement field induced on element **A** is $\mathbf{D} = \mathbf{d}\mathbf{T}$ where \mathbf{d} is the piezoelectric strain tensor. Consider only the electrical output generated on the planar surface of element **A** due to the out-of-plane piezoelectric responses, the generated polarization charge density on the planar surface of element **A** is $\rho_{\mathbf{A}} = d_{31}T \sin \phi + d_{32}T \cos \phi$. Similarly, the polarization charge density generated on the surface of element **B** is $\rho_{\mathbf{B}} = d_{31}T \cos \phi + d_{32}T \sin \phi$. The voltage generated on elements **A** and **B** can then be estimated based on a planar diode model, i.e. $V_{\mathbf{A},\mathbf{B}} = \rho_{\mathbf{A},\mathbf{B}}t/k\epsilon_0$ where t and k are the thickness and the out-of-plane electrostatic dielectric constant of the 2D piezoelectric material. To asses the performance of the directional stress sensing, we can define the *voltages response ratio* and the *differential*

voltage response as

$$\bar{V}_{AB}(\phi) \equiv \frac{V_{\mathbf{A}}}{V_{\mathbf{B}}} = \frac{\sin \phi + \xi \cos \phi}{\cos \phi + \xi \sin \phi}, \quad (13a)$$

$$\Delta V_{AB}(\phi) \equiv V_{\mathbf{A}} - V_{\mathbf{B}} = (d_{32} - d_{31}) \frac{Tt}{k\epsilon_0} (\cos \phi - \sin \phi). \quad (13b)$$

As $\bar{V}_{AB}(\phi)$ and $\Delta V_{AB}(\phi)$ are unique functions of ϕ , measuring one of them allows the mechanical stress direction ϕ to be unambiguously determined [e.g. see Fig. 7(d) for the angular plot of $\bar{V}_{AB}(\phi)$]. Interestingly, Eq. (13b) reveals the importance of having a sizable d_{32} in achieving sensitive directional mechanical stress sensing that is otherwise not achievable in non-Janus NbOX₂. Here ΔV_{AB} should be, ideally, as large as possible so to achieve good signal-to-noise ratio in the measurements. For materials with $d_{32} = 0$, $|\Delta V_{AB}(\phi)| \propto d_{31}$. In this case, a large d_{31} is required to achieve large ΔV_{AB} . In the contrary case of $d_{32} \neq 0$, the magnitude of the differential voltage follows $|\Delta V_{AB}(\phi)| \propto |d_{32} - d_{31}|$, thus suggesting that d_{32} offers an alternative route to achieve large $|\Delta V_{AB}(\phi)|$ for systems in which d_{31} is inherently small, such as Janus TMDC. To illustrate this aspect, we define the *maximum differential voltage response per unit stress* rescaled by k as $\tilde{\Delta V}_{AB}^{(\max)} \equiv k\Delta V_{AB}^{(\max)}/T$ where $\Delta V_{AB}^{(\max)}$ is the maximum of the magnitude of ΔV_{AB} evaluated at $\phi = 0$ or $\pi/2$. For NbOCIBr, NbOCII and

NbOBrI, $\Delta\tilde{V}_{AB}^{(\max)} = (0.10, 2.20, 1.63) \times 10^{-2}$ V/GPa, respectively. These values are significantly larger than the $\tilde{V}_{AB}^{(\max)} = 1.15 \times 10^{-3}$ V/GPa of Janus MoSeTe monolayer (thickness $t = 3.405$ Å [108]) in which only $d_{31} = 0.030$ pm/V is present. In general, to obtain the same $\Delta\tilde{V}_{AB}^{(\max)}$ of a piezoelectric material of thickness t' that possesses only d'_{31} , a piezoelectric materials with simultaneous d_{31} and d_{32} requires only

$$d_{31} = \frac{t'}{t} \frac{d'_{31}}{|\xi - 1|} \quad (14)$$

where $\xi \equiv d_{32}/d_{31}$. The presence of d_{32} (or equivalently ξ) relaxes the requirement of d_{31} and offer an alternative way to achieve sensitive directional sensing of mechanical stress. Taking NbOClI as an example, achieving the same $\Delta\tilde{V}_{AB}^{(\max)}$ would require a hypothetical piezoelectric material of the same thickness with a much larger $d_{32} \approx 0.48$ pm/V. The above analysis thus highlights the important role of the out-of-plane piezoelectric response d_{32} in supplementing the functionality and performance of 2D piezoelectric and piezoelectronic devices.

IV. CONCLUSION

In summary, we computationally demonstrated NbOXY monolayers as a stable and mechanically flexible 2D semiconductor family with exceptional electronic, piezoelectric, photocatalytic and optical properties. The high carrier mobility and the band gap value lying in the visible light regime of ~ 2 eV suggested the strong potential of NbOXY in electronic and optoelectronic device applications. The sizable in-plane (d_{11}) and two distinctive out-of-plane piezoelectric responses (d_{31} and d_{32}) greatly enhances the design flexibility of NbOXY-based devices. The strong linear optical dichroism in the visible-to-UV regime and the large optical absorption peak response in the deep UV regime revealed the capability of NbOXY in photonics device applications, such as polarizer and ultraviolet light photodetector. Finally, the high carrier mobility, sizable built-in electric field, strong optical absorption in the visible light regime, and the appropriate band edge energies that are compatible with overall water splitting suggested the potential of NbOXY in achieving high-performance solar-to-hydrogen conversion. Our findings unveiled NbOXY as an intriguing multifunctional 2D semiconductor family

with strong potential in electronics, optoelectronics, UV photonics, piezoelectronics and sustainable energy applications, and shall form a harbinger for the exploration of the broader 2D oxyhalides family towards next-generation advanced functional device technology.

AUTHOR CREDIT STATEMENT

Tong Su: Conceptualization, Methodology, Formal analysis, Investigation, Data Curation, Writing - Review & Editing. Ching Hua Lee: Investigation, Writing - Review & Editing. San-Dong Guo: Writing - Review & Editing. Guangzhao Wang: Formal analysis, Writing - Review & Editing. Wee-Liat Ong: Investigation, Writing - Review & Editing. Liemao Cao: Investigation, Writing - Review & Editing. Weiwei Zhao: Supervision, Writing - Review & Editing. Shengyuan A. Yang: Investigation, Writing - Review & Editing. Yee Sin Ang: Supervision, Project administration, Funding acquisition, Conceptualization, Formal analysis, Writing - Original Draft, Writing - Review & Editing, Visualization, Resources

DECLARATION OF COMPETING INTEREST

The authors declare that they have no known competing financial interests or personal relationships that could have appeared to influence the work reported in this paper.

DATA AVAILABILITY

Data will be made available on reasonable request.

ACKNOWLEDGEMENT

This work is funded by the Singapore University of Technology and Design (SUTD) Kickstarter Initiatives (SKI 2021_01_12) and SUTD-ZJU IDEA Visiting Professor Grant (SUTD-ZJU (VP) 202001). T. S. is supported by the China Scholarship Council (CSC). W. Z. is supported by the Natural Science Foundation of China (No. 52073075) and Shenzhen Science and Technology Program (Grant No. KQTD20170809110344233). The computational work for this article was partially performed on resources of the National Supercomputing Centre, Singapore (<https://www.nsc.sg>).

-
- [1] C. Cui, F. Xue, W.-J. Hu, L.-J. Li, Two-dimensional materials with piezoelectric and ferroelectric functionalities, *npj 2D Mater. Appl.* 2 (2018) 18.
 [2] M. Shehzad, S. Wang, Y. Wang, Flexible and transparent piezoelectric loudspeaker, *npj Flex. Electron.* 5 (2021) 24.

- [3] S. Bera, S. Guerin, H. Yuan, J. O'Donnell, N.P. Reynolds, O. Maraba, W. Ji, L.J.W. Shimon, P.-A. Cazade, S.A.M. Tofail, D. Thompson, R. Yang, E. Gazit, Molecular engineering of piezoelectricity in collagen-mimicking peptide assemblies, *Nat. Commun.* 12 (2021) 2634.

- [4] Q. Zhang, S. Zuo, P. Chen, C. Pan, Piezotronics in two-dimensional materials, *InfoMat* 3 (9) (2021) 987–1007.
- [5] A. Janshoff, H.-J. Galla, C. Steinem, Piezoelectric mass-sensing devices as biosensors—an alternative to optical biosensors?, *Angew. Chem. Int. Ed.* 39 (22) (2000) 4004–4032.
- [6] A. I. Kingon, S. Srinivasan, Lead zirconate titanate thin films directly on copper electrodes for ferroelectric, dielectric and piezoelectric applications, *Nat. Mater.* 4 (3) (2005) 233–237.
- [7] Z. L. Wang, J. Song, Piezoelectric nanogenerators based on zinc oxide nanowire arrays, *Science* 312 (5771) (2006) 242–246.
- [8] S. C. Masmanidis, R. B. Karabalin, I. De Vlaminck, G. Borghs, M. R. Freeman, M. L. Roukes, Multifunctional nanomechanical systems via tunably coupled piezoelectric actuation, *Science* 317 (5839) (2007) 780–783.
- [9] W. Wu, Z. L. Wang, Piezotronics and piezophotonics for adaptive electronics and optoelectronics, *Nat. Rev. Mater.* 1 (2016) 16031.
- [10] A. Khan, Z. Abas, H. S. Kim, I.-K. Oh, Piezoelectric thin films: an integrated review of transducers and energy harvesting, *Smart Mater. Struct.* 25 (5) (2016) 053002.
- [11] S. Wang, F. Cao, Y. Wu, X. Zhang, J. Zou, Z. Lan, W. Sun, J. Wu, P. Gao, Multifunctional 2D perovskite capping layer using cyclohexylmethylammonium bromide for highly efficient and stable perovskite solar cells, *Mater. Today Phys.* 21 (2021) 100543.
- [12] S. Zhi, J. Jia, Q. Zhang, F. Cao, X. Liu, J. Mao, A sketch for super-thermoelectric materials, *Mater. Today Phys.* 22 (2022) 100618.
- [13] F.-R. Feng, Z.-Q. Tian, Z. L. Wang, Flexible triboelectric generator, *Nano Energy* 1 (2) (2012) 328–334.
- [14] W. Wu, L. Wang, Y. Li, F. Zhang, L. Lin, S. Niu, D. Chenet, X. Zhang, Y. Hao, T. F. Heinz, J. Hone, Z. Wang, Piezoelectricity of single-atomic-layer MoS_2 for energy conversion and piezotronics, *Nature* 514 (7523) (2014) 470–474.
- [15] S. Gupta, S. N. Shirodkar, A. Kutana, B. I. Yn, In pursuit of 2D materials for maximum optical response, *ACS Nano* 12 (11) (2018) 10880–10889.
- [16] R. Li, Y. Cheng, W. Huang, Recent progress of janus 2D transition metal chalcogenides: from theory to experiments, *Small* 14 (45) (2018) 1802091.
- [17] A. Pal, S. Zhang, T. Chavan, K. Agashiwala, C.-H. Yeh, W. Cao, K. Banerjee, Quantum-engineered devices based on 2D material for next-generation information processing and storage, *Adv. Mater.* n/a (n/a) (2022) 2109894.
- [18] P. V. Pham, S. C. Bodepudi, K. Shehzad, Y. Liu, Y. Xu, B. Yu, X. Duan, 2d heterostructures for ubiquitous electronics and optoelectronics: Principles, opportunities, and challenges, *Chem. Rev.* 122 (6) (2022) 6514–6613.
- [19] G. Cheon, K.-A. N. Duerloo, A. D. Sendek, C. Porter, Y. Chen, E. J. Reed, Data mining for new two- and one-dimensional weakly bonded solids and lattice-commensurate heterostructures, *Nano Lett.* 17 (3) (2017) 1915–1923.
- [20] K.-A. N. Duerloo, M. T. Ong, E. J. Reed, Intrinsic piezoelectricity in two-dimensional materials, *J. Phys. Chem. Lett.* 3 (19) (2012) 2871–2876.
- [21] H. Zhu, Y. Wang, J. Xiao, M. Liu, S. Xiong, Z. J. Wong, Z. Ye, Y. Ye, X. Yin, X. Zhang, Observation of piezoelectricity in free-standing monolayer MoS_2 , *Nat. Nanotechnol.* 10 (2) (2015) 151–155.
- [22] S. K. Kim, R. Bhatia, T.-H. Kim, D. Seol, J. H. Kim, H. Kim, W. Seung, Y. Kim, Y. H. Lee, S.-W. Kim, Directional dependent piezoelectric effect in CVD grown monolayer MoS_2 for flexible piezoelectric nanogenerators, *Nano Energy* 22 (2016) 483–489.
- [23] J. Lee, J. Y. Park, E. B. Cho, T. Y. Kim, S. A. Han, T. Kim, Y. Liu, S. K. Kim, J. R. Chang, H. Yoon, Reliable piezoelectricity in bilayer WSe_2 for piezoelectric nanogenerators, *Adv. Mater.* 29 (29) (2017).
- [24] J. Qi, Y. W. Lan, A. Z. Stieg, J. H. Chen, Y. L. Zhong, L. J. Li, C. D. Chen, Y. Zhang, K. L. Wang, Piezoelectric effect in chemical vapour deposition-grown atomic-monolayer triangular molybdenum disulfide piezotronics, *Nat. Commun.* 6 (2015) 7430.
- [25] K. Michel and B. Verberck, Theory of elastic and piezoelectric effects in two-dimensional hexagonal boron nitride, *Phys. Rev. B* 80 (22) (2009) 224310.
- [26] M. Zelisko, Y. Hanlumuayang, S. Yang, Y. Liu, C. Lei, J. Li, P. M. Ajayan, P. Sharma, Anomalous piezoelectricity in two-dimensional graphene nitride nanosheets, *Nat. Commun.* 5 (1) (2014) 4284.
- [27] G. da Cunha Rodrigues, P. Zelenovskiy, K. Romanyuk, S. Luchkin, Y. Kopelevich, A. Kholkin, Strong piezoelectricity in single-layer graphene deposited on SiO_2 grating substrates, *Nat. Commun.* 6 (1) (2015) 7572.
- [28] H.-J. Jin, W. Y. Yoon, W. Jo, Virtual out-of-plane piezoelectric response in MoS_2 layers controlled by ferroelectric polarization, *ACS Appl. Mater. Interfaces* 10 (1) (2018) 1334–1339.
- [29] A.-Y. Lu, H. Zhu, J. Xiao, C.-P. Chuu, Y. Han, M.-H. Chiu, C.-C. Cheng, C.-W. Yang, K.-H. Wei, Y. Yang, Y. Wang, D. Sokaras, D. Nordlund, P. Yang, D. A. Muller, M.-Y. Chou, X. Zhang, L.-J. Li, Janus monolayers of transition metal dichalcogenides, *Nat. nanotechnol.* 12 (8) (2017) 744–749.
- [30] L. Dong, J. Lou, V. B. Shenoy, Large in-plane and vertical piezoelectricity in janus transition metal dichalcogenides, *ACS Nano* 11 (8) (2017) 8242–8248.
- [31] S.-D. Guo, X.-K. Feng, Y.-T. Zhu, G. Wang, S. A. Yang, Two-dimensional janus Si dichalcogenides: A first-principles study, (2022) 05027 arXiv:2209.
- [32] Z. Chang, W. Yan, J. Shang, J. Z. Liu, Piezoelectric properties of graphene oxide: A first-principles computational study, *Appl. Phys. Lett.* 105 (2) (2014) 023103.
- [33] J. Shi, C. Han, X. Wang, S. Yun, Electronic, elastic and piezoelectric properties of boron-V group binary and ternary monolayers, *Phys. B: Condens. Matter.* 574 (2019) 311634.
- [34] R. Hinchet, U. Khan, C. Falconi, S.-W. Kim, Piezoelectric properties in two-dimensional materials: Simulations and experiments, *Mater. Today* 21 (6) (2018) 611–630.
- [35] Y. Guo, S. Zhou, Y. Bai, J. Zhao, Enhanced piezoelectric effect in janus group-III chalcogenide monolayers, *Appl. Phys. Lett.* 110 (16) (2017) 163102.
- [36] S.-J. Liang, B. Cheng, X. Cui, F. Miao, Van der waals heterostructures for high-performance device applications: challenges and opportunities, *Adv. Mater.* 32 (27) (2020) 1903800.

- [37] J. Zhou, L. Shen, M. D. Costa, K. A. Persson, S. P. Ong, P. Huck, Y. Lu, X. Ma, Y. Chen, H. Tang, Y. P. Feng, 2Dmatpedia, an open computational database of two-dimensional materials from top-down and bottom-up approaches, *Sci. data.* 6 (1) (2019) 86.
- [38] Y. Wu, I. Abdelwahab, K. C. Kwon, I. Verzhbitskiy, L. Wang, W. H. Liew, K. Yao, G. Eda, K. P. Loh, L. Shen, S. Y. Quek, Data-driven discovery of high performance layered van der waals piezoelectric *NbOI₂*, *Nat. Commun.* 13 (2022) 1884.
- [39] Y. Fang, F. Wang, R. Wang, T. Zhai, F. Huang, 2D *NbOI₂*: A chiral semiconductor with highly in-plane anisotropic electrical and optical properties, *Adv. Mater.* 33 (29) (2021) 2101505.
- [40] I. Abdelwahab, B. Tilmann, Y. Wu, D. Giovanni, I. Verzhbitskiy, M. Zhu, R. Berté, F. Xuan, L. d. S. Menezes, G. Eda, T. C. Sum, S. Y. Quek, S. A. Maier, K. P. Loh, Giant second-harmonic generation in ferroelectric *NbOI₂*, *Nat. Photonics* 16 (9) (2022) 644–650.
- [41] Y. Jia, M. Zhao, G. Gou, X. C. Zeng, J. Li, Niobium oxide dihalides *NbOX₂*: a new family of two-dimensional van der waals layered materials with intrinsic ferroelectricity and antiferroelectricity, *Nanoscale Horizons* 4 (5) (2019) 1113–1123.
- [42] Q. Ye, Y.-H. Shen, C.-G. Duan, Ferroelectric controlled spin texture in two-dimensional *NbOI₂* monolayer, *Chin. Phys. Lett.* 38 (8) (2021) 087702.
- [43] B. Mortazavi, M. Shahrokhi, B. Javvaji, A. V. Shapeev, X. Zhuang, Highly anisotropic mechanical and optical properties of 2D *NbOX₂* (X= Cl, Br, I) revealed by first-principle, *Nanotechnol.* 33 (27) (2022) 275701.
- [44] J. Zhao, W. Wu, J. Zhu, Y. Lu, B. Xiang, S. A. Yang, Highly anisotropic two-dimensional metal in monolayer *MoOCl₂*, *Phys. Rev. B* 102 (24) (2020) 245419.
- [45] Z. Wang, M. Huang, J. Zhao, C. Chen, H. Huang, X. Wang, P. Liu, J. Wang, J. Xiang, C. Feng, Z. Zhang, X. Cui, Y. Lu, S. A. Yang, B. Xiang, *Phys. Rev. Mater.* 4 (4) (2020) 041001(R).
- [46] H. Qu, S. Guo, W. Zhou, Z. Wu, J. Cao, Z. Li, H. Zeng, S. Zhang, Enhanced interband tunneling in two-dimensional tunneling transistors through anisotropic energy dispersion, *Phys. Rev. B* 105 (7) (2022) 075413.
- [47] M. Sun, Y. Luo, Y. Yan, U. Schwingenschlogl, Ultrahigh carrier mobility in the two-dimensional semiconductors *B₈Si₄*, *B₈Ge₄*, and *B₈Sn₄*, *Chem. Mater.* 33 (16) (2021) 6475–6483.
- [48] Y. Zhao, J. Qiao, Z. Yu, P. Yu, K. Xu, S. P. Lau, W. Zhou, Z. Liu, X. Wang, W. Ji, Y. Chai, High-electron-mobility and air-stable 2D layered *PtSe₂* FETs, *Adv. Mater.* 29 (5) (2017) 1604230.
- [49] H. R. Banjade, J. Pan, Q. Yan, Monolayer 2D semiconducting tellurides for high-mobility electronics, *Phys. Rev. Mater.* 5 (1) (2021) 014005.
- [50] C. Zhang, R. Wang, H. Mishra, Y. Liu, Discovering 2D semiconductors with high intrinsic carrier mobility at room temperature, (2022) 10663 arXiv:2208.
- [51] Z. Li, B. Li, X. Wu, S. A. Sheppard, S. Zhang, D. Gao, N. J. Long, Z. Zhu, Organometallic-functionalized interfaces for highly efficient inverted perovskite solar cells, *Science* 376 (6591) (2022) 416–420.
- [52] M. Xie, S. Zhang, B. Cai, Y. Huang, Y. Zou, B. Guo, Y. Gu, H. Zeng, A promising two-dimensional solar cell donor: Black arsenic–phosphorus monolayer with 1.54 eV direct bandgap and mobility exceeding 14,000 cm² V⁻¹s⁻¹, *Nano Energy* 28 (2016) 433–439.
- [53] B. Cai, M. Xie, S. Zhang, C. Huang, E. Kan, X. Chen, Y. Gu, H. Zeng, A promising two-dimensional channel material: monolayer antimonide phosphorus, *Sci. China Mater.* 59 (8) (2016) 648–656.
- [54] W.-Z. Xiao, G. Xiao, Q.-Y. Rong, and L.-L. Wang, New two-dimensional V–V binary compounds with a honeycomb-like structure: a first-principles study, *Mater. Res. Express* 5(3) (2018) 035903.
- [55] W. Xu, Y. Jin, B. Zheng, H. Xu, Extremely high mobilities in two-dimensional group-VA binary compounds with large conversion efficiency for solar cells, *J. Phys. Chem. C* 122 (48) (2018) 27590–27596.
- [56] M. Wang, L. Fan, Y. Qiu, D. Chen, X. Wu, C. Zhao, J. Cheng, Y. Wang, N. Zhang, K. Sun, Electrochemically active separators with excellent catalytic ability toward high-performance Li–S batteries, *J. Mater. Chem.* 6 (25) (2018) 11694–11699.
- [57] S. Kaushik and R. Singh, 2D layered materials for ultraviolet photodetection: A review, *Adv. Opt. Mater.* 9 (11) (2021) 2002214.
- [58] X. Gan, D. Lei, K.-Y. Wong, Two-dimensional layered nanomaterials for visible–light–driven photocatalytic water splitting, *Mater. Today Energy* 10 (2018) 352–367.
- [59] P. Hohenberg, W. Kohn, Inhomogeneous electron gas, *Phys. Rev.* 136 (3B) (1964) B864.
- [60] W. Kohn, L. J. Sham, Self-consistent equations including exchange and correlation effects, *Phys. Rev.* 140 (4A) (1965) A1133.
- [61] G. Kresse, J. Hafner, 14251; g. kresse, j. furthmüller, *Phys. Rev. B* 54 (1996) 11169.
- [62] G. Kresse, J. Hafner, Norm-conserving and ultrasoft pseudopotentials for first-row and transition elements, *J. Condens. Matter Phys.* 6 (40) (1994) 8245.
- [63] J. Tao, J. P. Perdew, H. Tang, and C. Shahi, Origin of the size-dependence of the equilibrium van der waals binding between nanostructures, *J. Chem. Phys.* 148 (7) (2018) 074110.
- [64] G. Heyd, Scuseria, and M. Ernzerhof, *J. Chem. Phys.* 118 (18) (2003) 8270.
- [65] A. V. Krukau, O. A. Vydrov, A. F. Izmaylov, and G. E. Scuseria, Influence of the exchange screening parameter on the performance of screened hybrid functionals, *J. Chem. Phys.* 125 (22) (2006) 224106.
- [66] V. Wang, N. Xu, J.-C. Liu, G. Tang, W.-T. Geng, Vaspkit: A user-friendly interface facilitating high-throughput computing and analysis using vasp code, *Comput. Phys. Commun.* 267 (2021) 108033.
- [67] G. Henkelman, A. Arnaldsson, H. Jónsson, A fast and robust algorithm for bader decomposition of charge density, *Comput. Mater. Sci.* 36 (3) (2006) 354–360.
- [68] J. Bardeen, W. Shockley, Deformation potentials and mobilities in non-polar crystals, *Phys. Rev.* 80 (1950) 72–80.
- [69] Y. Wu, C. Ma, Y. Chen, B. Mortazavi, Z. Lu, X. Zhang, K. Xu, H. Zhang, W. Liu, T. Rabczuk, H. Zhu, Z. Fang, R. Zhang, New group V graphyne: two-dimensional direct semiconductors with remarkable carrier mobilities, thermoelectric performance, and thermal stability, *Mater. Today Phys.* 12 (2020) 100164.
- [70] S. Baroni, S. De Gironcoli, A. Dal Corso, P. Giannozzi, Phonons and related crystal properties from density-functional perturbation theory, *Rev. Mod. Phys.* 73 (2)

- (2001) 515.
- [71] A. Togo, F. Oba, I. Tanaka, First-principles calculations of the ferroelastic transition between rutile-type and cacl 2-type SiO_2 at high pressures, *Phys. Rev. B* 78 (13) (2008) 134106.
- [72] N. Shuichi, Constant temperature molecular dynamics methods, *Prog. Theor. Phys.* 103 (1991) 1–46.
- [73] X. Wu, D. Vanderbilt, D. Hamann, Systematic treatment of displacements, strains, and electric fields in density-functional perturbation theory, *Phys. Rev. B* 72 (3) (2005) 035105.
- [74] M. N. Blonsky, H. L. Zhuang, A. K. Singh, R. G. Hennig, Ab initio prediction of piezoelectricity in two-dimensional materials, *ACS nano* 9 (10) (2015) 9885–9891.
- [75] M. de Jong, W. Chen, H. Geerlings, M. Asta, K. A. Persson, A database to enable discovery and design of piezoelectric materials, *Sci. Data* 2 (2015) 150053.
- [76] M. De Jong, W. Chen, H. Geerlings, M. Asta, K. A. Persson, A database to enable discovery and design of piezoelectric materials, *Sci. Data* 2 (1) (2015) 150053.
- [77] R. Hill, The elastic behaviour of a crystalline aggregate, *Proc. Phys. Soc. A* 65 (5) (1952) 349.
- [78] M. Liao, Y. Liu, L. Min, Z. Lai, T. Han, D. Yang, J. Zhu, Alloying effect on phase stability, elastic and thermodynamic properties of Nb-Ti-V-Zr high entropy alloy, *Intermetallics* 101 (2018) 152–164.
- [79] M. Liao, Y. Liu, P. Cui, N. Qu, F. Zhou, D. Yang, T. Han, Z. Lai, J. Zhu, Modeling of alloying effect on elastic properties in Bcc Nb-Ti-V-Zr solid solution: From unary to quaternary, *Comput. Mater. Sci.* 172 (2020) 109289.
- [80] C. Jasiukiewicz, T. Paszkiewicz, S. Wolski, Fourth-rank tensors of $[[v_2]_2]$ - type and elastic material constants for 2D crystals, *Phys. Status Solidi B* 245 (3) (2008) 557–561.
- [81] D. Bohm, D. Pines, A collective description of electron interactions. I. magnetic interactions, *Phys. Rev.* 82 (5) (1951) 625.
- [82] H. Ehrenreich, M. H. Cohen, Self-consistent field approach to the many-electron problem, *Phys. Rev.* 115 (4) (1959) 786.
- [83] M. Shishkin, G. Kresse, Implementation and performance of the frequency-dependent GW method within the PAW framework, *Phys. Rev. B* 74 (3) (2006) 035101.
- [84] E. E. Salpeter, H. A. Bethe, A relativistic equation for bound-state problems, *Phys. Rev.* 84 (6) (1951) 1232.
- [85] G. Onida, L. Reining, A. Rubio, Electronic excitations: density-functional versus many-body green’s-function approaches, *Rev. Mod. Phys.* 74 (2) (2002) 601.
- [86] M. Mazdziarz, Comment on ‘The Computational 2D Materials Database: high-throughput modeling and discovery of atomically thin crystals’, *2D Mater.* 6 (2019) 048001.
- [87] T. V. Vu, C. V. Nguyen, H. V. Phuc, A. A. Lavrentyev, O. Y. Khyzhun, N. V. Hieu, M. M. Obeid, D. P. Rai, H. D. Tong, N. N. Hieu, Theoretical prediction of electronic, transport, optical, and thermoelectric properties of janus monolayers in_2xO ($x = \text{S}, \text{Se}, \text{Te}$), *Phys. Rev. B* 103 (2021) 085422.
- [88] G.-Z. Wang, J.-L. Chang, W. Tang, W. Xie, Y. S. Ang, 2d materials and heterostructures for photocatalytic water-splitting: A theoretical perspective, *J. Phys. D: Appl. Phys.* 55 (29) (2022) 293002.
- [89] Y. Ji, M. Yang, H. Lin, T. Hou, L. Wang, Y. Li, S.-T. Lee, Janus structures of transition metal dichalcogenides as the heterojunction photocatalysts for water splitting, *J. Phys. Chem. C* 122 (5) (2018) 3123–3129.
- [90] M. M. Obeid, C. Stampfl, A. Bafekry, Z. Guan, H. Jappor, C. Nguyen, M. Naseri, D. Hoat, N. Hieu, A. Krauklis, T. V. Vu, D. Gogova, First-principles investigation of nonmetal doped single-layer biobr as a potential photocatalyst with a low recombination rate, *Phys. Chem. Chem. Phys.* 22 (27) (2020) 15354–15364.
- [91] J. Li, W. Zhou, L. Xu, J. Yang, H. Qu, T. Guo, B. Xu, S. Zhang, H. Zeng, Revealing the weak fermi level pinning effect of 2D semiconductor/2D metal contact: A case of monolayer $\text{In}_2\text{Ge}_2\text{Te}_6$ and its janus structure $\text{In}_2\text{Ge}_2\text{Te}_3\text{Se}_3$, *Mater. Today Phys.* (2022) 100749.
- [92] H. Yuan, J. Su, P. Zhang, Z. Lin, J. Zhang, J. Zhang, J. Chang, Y. Hao, Tuning the intrinsic electric field of janus-TMDs to realize high-performance $\beta\text{-Ga}_2\text{O}_3$ device based on $\beta\text{-Ga}_2\text{O}_3$ /janus-TMD heterostructures, *Mater. Today Phys.* 21 (2021) 100549.
- [93] D. S. Chong, J. J. Foo, X.-Q. Tan, G. Z. S. Ling, L.-L. Tan, X. Chen, W.-J. Ong, Evolutionary face-to-face 2D/2D bismuth-based heterojunction: The quest for sustainable photocatalytic applications, *Appl. Mater. Today* 29 (2022) 101636.
- [94] Y. Lv, P. Chen, J. Foo, J. Zhang, W. Qian, C. Chen, W.-J. Ong, Dimensionality-dependent MoS_2 toward efficient photocatalytic hydrogen evolution: from synthesis to modifications in doping, surface and heterojunction engineering, *Mater. Today Nano* 18 (2022) 100191.
- [95] C. Herring, Transport properties of a many-valley semiconductor, *Bell Syst. Tech. J.* 34 (2) (1955) 237–190.
- [96] K. Blotekjaer, Transport equations for electrons in two-valley semiconductors, *IEEE Trans. Electron. Devices* 17 (1) (1970) 38–47.
- [97] J. Zhao, D. Ma, C. Wang, Z. Guo, B. Zhang, J. Li, G. Nie, N. Xie, H. Zhang, Recent advances in anisotropic two-dimensional materials and device applications, *Nano Res.* 14 (4) (2021) 897–919.
- [98] S. Puebla, R. D’Agosta, G. Sanchez-Santolino, R. Frisenda, C. Munuera, A. Castellanos-Gomez, In-plane anisotropic optical and mechanical properties of two-dimensional MoO_3 , *npj 2D Mater. Appl.* 5 (1) (2021) 37.
- [99] H. Jiang, L. Zheng, Z. Liu, X. Wang, Two-dimensional materials: From mechanical properties to flexible mechanical sensors, *InfoMat* 2 (6) (2020) 1077–1094.
- [100] R. Peng, Y. Ma, Q. Wu, B. Huang, Y. Dai, Two-dimensional materials with intrinsic auxeticity: progress and perspectives, *Nanoscale* 11 (24) (2019) 11413–11428.
- [101] M. E. Kilic, K.-R. Lee, Emerging exotic properties of two-dimensional ternary tetrahedral BCN: Tunable anisotropic transport properties with huge excitonic effects for nanoelectronics and optoelectronics, *Mater. Today Phys.* 27 (2022) 100792.
- [102] M. Bernardi, M. Palummo, J. C. Grossman, Extraordinary sunlight absorption and one nanometer thick photovoltaics using two-dimensional monolayer materials, *Nano Lett.* 13 (8) (2013) 3664–3670.
- [103] H. Meng, L.-L. Wang, C. H. Lee, Y. S. Ang, Terahertz Polarization Conversion from Optical Dichroism in a Topological Dirac Semimetal, *Appl. Phys. Lett.* 121 (19) in press (2022).

- [104] Y. Fang, F. Wang, R. Wang, T. Zhai, F. Huang, 2d nb₂: A chiral semiconductor with highly in-plane anisotropic electrical and optical properties, *Adv. Mater.* 33 (29) (2021) 2101505.
- [105] X. Wang, Y. Li, L. Huang, X.-W. Jiang, L. Jiang, H. Dong, Z. Wei, J. Li, W. Hu, Short-wave near-infrared linear dichroism of two-dimensional germanium selenide, *J. Am. Chem. Soc.* 139 (42) (2017) 14976–14982.
- [106] J. Qiao, X. Kong, Z. Hu, Few layered black phosphorus: emerging 2D semiconductor with high anisotropic carrier mobility and linear dichroism, *Nat. Commun.* 5 (2014) 4475.
- [107] L.-S. Lu, G.-H. Chen, H.-Y. Cheng, C.-P. Chuu, K.-C. Lu, C.-H. Chen, M.-Y. Lu, T.-H. Chuang, D.-H. Wei, W.-C. Chueh, W.-B. Jian, M.-Y. Li, Y.-M. Chang, L.-J. Li, W.-H. Chang, Layer-dependent and in-plane anisotropic properties of low-temperature synthesized few-layer *PdSe₂* single crystals, *ACS Nano* 14 (4) (2020) 4963–4972.
- [108] X. Yang, D. Singh, Z. Xu, Z. Wang, R. Ahuja, An emerging Janus MoSeTe material for potential applications in optoelectronic devices, *J. Mater. Chem. C* 7 (39) (2019) 12312–12320.